

# Peruvian Altiplano stratigraphy highlights along-strike variability in foreland basin evolution of the Cenozoic central Andes

Kurt E. Sundell<sup>1,2†</sup>

Joel E. Saylor<sup>1</sup>

Thomas J. Lapen<sup>1</sup>

Richard H. Styron<sup>3,4,5</sup>

Dustin Villarreal<sup>1</sup>

Paola Usnayo<sup>6</sup>

José Cárdenas<sup>6</sup>

<sup>1</sup>*Department of Earth and Atmospheric Sciences, University of Houston, Houston, Texas, USA*

<sup>2</sup>*Now at Department of Geosciences, University of Arizona, Tucson, AZ 85721, USA*

<sup>3</sup>*Earth Analysis, Los Gatos, CA, USA*

<sup>4</sup>*Global Earthquake Model Foundation, Pavia, Italy*

<sup>5</sup>*Department of Geology, University of Kansas, Lawrence, KS 66054 USA*

<sup>6</sup>*Departamento Académico de Geología, Universidad San Antonio Abad del Cusco, Cusco, Peru*

<sup>†</sup>*Corresponding author: sundell@email.arizona.edu*

## Keywords

Central Andean Plateau, sediment provenance, detrital zircon, flexure, orogenic cyclicity

This article has been accepted for publication and undergone full peer review but has not been through the copyediting, typesetting, pagination and proofreading process which may lead to differences between this version and the Version of Record. Please cite this article as doi: 10.1029/2017TC004775

## ABSTRACT

Retroarc foreland basins in the Andean plateau contain critical information on geodynamic processes driving plateau development by providing a record of exhumation and sediment sourcing, as well as the timing, location, and magnitude of basin subsidence. However, this record is incomplete along orogenic strike, and particularly limited in southern Peru. We measured ~6200 m of non-marine clastic strata in the northern Peruvian Altiplano, documented through lithofacies characterization and paleocurrent analysis, conglomerate clast counts, sandstone petrography, and detrital zircon U-Pb geochronology; for the latter we employ quantitative detrital zircon interpretation methods including multidimensional scaling, mixture modeling, and quantification of zircon roundness. Results show dominant sediment sourcing from the Western Cordillera and/or western Altiplano. Sediment accumulation rates define an upward-convex Paleogene subsidence profile consistent with deposition in a northeastward-migrating flexural foreland basin system, with lithospheric loading from an increasingly proximal Western Cordilleran hinterland. Basin deposition following a 23–9 Ma angular unconformity shows a marked increase in sediment accumulation rates > 800 m/Myr, interpreted as a departure from flexural subsidence. Results highlight along-strike variability in Andean foreland basin evolution, as foredeep deposits are thicker, and the onset of rapid sediment accumulation occurs earlier in southern Peru compared to Bolivia and Argentina. Results tentatively support models of orogenic cyclicity, and reveal that episodes of high-flux magmatism in southern Peru are slightly out of phase with those documented in northwest Argentina, which may be controlled by preexisting Paleozoic–Mesozoic structural and stratigraphic fabrics and the rate of underthrusted melt-fertile continental lower crust and mantle lithosphere.

## 1. INTRODUCTION

Cenozoic basins archive the ongoing development of the central Andes, and development of the Andean plateau, Earth's second largest modern orogenic plateau (Jordan et al., 1983; Allmendinger et al., 1997) (Figure 1a). Protracted subduction of the Nazca oceanic plate beneath the South American continent resulted in mountain building, and generation of the low relief, high-elevation topography of the Altiplano. Nearly continuous, non-marine sedimentation during the Cenozoic records the Andean deformational history in the Altiplano-Puna plateau, which is characterized by high (~3800 m average) elevation, dominantly internal drainage, and relatively subdued relief compared to the higher elevation, more rugged terrains of the adjacent Western Cordilleran magmatic arc and Eastern Cordilleran fold-and-thrust belt (Figure 1b).

Early records of cross-cutting and stratigraphic relationships in this region set the foundation for, and continue to shape our current understanding of Andean plateau formation (e.g., Forbes, 1861; Berry, 1917; Newell, 1946, 1949). Although there is a general consensus that the Andean plateau formed in the Cenozoic (e.g., Jordan et al., 1983; Isacks, 1988; Allmendinger et al., 1997), debates persist on the relative timing of different geodynamic processes controlling its formation (e.g., Barnes & Ehlers, 2009; Ehlers & Poulsen, 2009). For example, models calling solely on crustal shortening to explain regional elevation gain (e.g., Baby, 1997; Lamb, 2011) are typically at odds with models of plateau formation that involve a decoupling of surface uplift and crustal shortening (e.g., Garzione et al., 2006, 2008; Saylor & Horton, 2014; Kar et al., 2016). Critical to addressing such questions are records of basin subsidence, surface uplift, and crustal deformation at different locations along orogenic strike. However, such records in the northern part of the Andean plateau in southern Peru have largely been obscured by volcanic rocks from periods of intense magmatism (e.g., Mamani et al., 2008, 2010; Demouy et al., 2012), or complicated by

potential deformational overprinting during periods of oblique convergence (Carlotto, 2013) and contractional reactivation preexisting structures (e.g., Perez et al., 2016a). Cenozoic strata in the Peruvian Altiplano provide a valuable, yet relatively unexplored record of tectonic processes active during the Cenozoic construction of the Andean plateau.

Despite hosting a nearly complete record of Cenozoic strata chronicling the mountain building history of the central Andes, the northernmost Altiplano of southern Peru has received less research focus compared to its central and southern counterparts in Bolivia, Chile, and Argentina (e.g., Newell, 1946, 1949; Horton et al., 2001, 2002; DeCelles and Horton, 2003; Carrapa et al., 2012). While recent work in southern Peru has focused on the Eocene–Miocene sedimentary record by highlighting prolonged basin subsidence, episodes of punctuated deformation, and a broadly similar structural style of deformation and basin development to the Altiplano of Bolivia (Carlotto, 2013; Perez & Horton, 2014; Horton et al., 2015), geodynamic implications of foreland basin system development in the northernmost reaches of the Peruvian Altiplano have not been thoroughly addressed.

We present new sediment provenance data in the context of ~6200 m of non-marine siliciclastic strata to address the Cenozoic tectonic history of this part of the central Andes. Provenance indicators from paleocurrent measurements, conglomerate clast counts, sandstone petrography, multidimensional scaling and mixture modeling of detrital zircon U-Pb data, and quantification of zircon roundness, all suggest dominant sediment sourcing from the Peruvian Western Cordillera and/or western Altiplano throughout the Cenozoic, and limited evidence for input from the Eastern Cordillera. Detrital zircon mixture modeling using DZmix (Sundell & Saylor, 2017) elucidates brief pulses of Ordovician-age sediment input at ~36 and ~7 Ma, and is interpreted as timing of shortening-related exposure of Paleozoic stratigraphic formations in hanging wall thrust blocks. Mixture modeling further highlights the important role sediment recycling plays in this region. The presence of an angular

unconformity from 23–9 Ma is consistent with previously documented periods of deformation along strike to the south (Perez & Horton, 2014; Horton et al., 2015). When combined with sediment provenance indicators, results are consistent with the development and northeastward migration of a flexural foreland basin system (*sensu* DeCelles & Giles, 1996). Details of this system provide predictive power for local and regional geodynamic processes, in particular the timing and location of hinterland loading due to crustal thickening and/or surface uplift in the Western Cordillera, and basin subsidence to the east. Further, results provide a comparison to previously documented foreland systems in the modern Altiplano and Eastern Cordillera along strike to the south (e.g., Horton et al., 2001, 2002, 2015; DeCelles & Horton, 2003; DeCelles et al., 2011), and reveal an apparent southward younging in the onset of high sedimentation and accommodation rates resulting in thicker stratigraphic packages later in the process of foreland basin system evolution. Finally, consideration of the results of this research in the context of published records of magmatism, igneous geochemistry, and limited records of crustal shortening and surface uplift, collectively support models calling on cyclical orogenic processes (e.g., DeCelles et al., 2009; Ramos, 2009; Ramos et al., 2014; DeCelles et al., 2015), but highlight major temporal differences in the onset and tempo of cyclicity along orogenic strike.

## 2. GEOLOGIC BACKGROUND

The Pacific margin of the South American continent has undergone continuous ocean-continent convergence since at least the late Paleozoic resulting in Earth's longest modern continuous mountain chain (Allmendinger et al., 1983), and development of the Andean plateau, the most prominent modern topographic feature associated with ocean-continent convergence. Despite long-lived subduction and the protracted magmatic and tectonic history of the region (e.g., Chew et al., 2007; Bahlburg et al., 2011), the Andean plateau developed in the Cenozoic, and in the absence of any significant continental collision (Jordan et al., 1983;

Allmendinger et al., 1997). The Andean plateau is defined as the broad area of high ( $> 3$  km) topography in the central Andes that stretches north-south approximately 1800 km from southern Peru to northern Argentina, and east-west 350–400 km at its widest across Bolivia (Isacks, 1988) (Figure 1a). This region can be divided into physiographic regions, which from west to east are: i) the Precordillera, representing the modern interface between the subducting Nazca oceanic plate and the South American continent; ii) the active volcanic arc in the Western Cordillera; iii) the broad and relatively flat-lying and internally drained region that defines the Altiplano; iv) the rugged and high elevation terrain in the Eastern Cordillera; and v) the modern Subandean zone retroarc fold-and-thrust belt and associated flexural foredeep to the east (Figure 1b).

## 2.1. Tectonic history and sediment recycling

Determining sediment sources for the Cenozoic Altiplano is complicated by a tectonic history featuring multiple episodes of sedimentary rock formation and subsequent exhumation and recycling. The oldest ( $> 1200$  Ma) potential sediment source areas in southern Peru are basement rocks of the Arequipa Massif along the Pacific coast of the Precordillera, and rocks of the Amazonian craton to the east (e.g., Chew et al., 2007, 2008; Bahlburg et al., 2009, 2011; Reimann et al., 2010). Sediments from these areas were widely dispersed across the region during the Mesoproterozoic Sunsás-Grenville orogeny (1200–900 Ma) (Bahlburg et al., 2011). Sediments of middle Neoproterozoic–early Paleozoic age (750–500 Ma) may originate from subduction-related orogenesis at a Proto-Andean margin (Chew et al., 2008), or from the Brazilian shield farther east (Reimann et al., 2010).

Ordovician to recent stratigraphic formations incorporate sediments derived from rocks formed and exposed during the tectonic events mentioned above, and from eroded magmatic intrusions and volcanic deposits in the middle Mesozoic to Pleistocene. Deformation, reworking, and dispersal of sediments occurred during the 500–400 Ma

Famatinian orogeny, which also produced new source signatures from subduction-related magmatism that stretched continuously along the western edge of South America from modern Patagonia through Argentina to Venezuela (Chew et al., 2007). A Permian–Triassic back-arc extensional episode in southeastern Peru resulted in formation of the regionally-extensive, up to 3 km thick Mitu Group, as well as emplacement of multiple Triassic intrusive complexes (Kontak et al., 1990). Continued convergence between the Nazca and South American plates resulted in abundant arc magmatism in the early Jurassic (200–175 Ma), late Cretaceous–early Paleocene (90–60 Ma) (Demouy et al., 2012), and throughout the Cenozoic (65 Ma – present) (Mamani et al., 2010).

## 2.2. Study area

The most complete package of Cenozoic strata exposed in the northern Altiplano is located just south of Cusco, Peru (Figures 1c and 2). Preserved Cenozoic sedimentary basins are bounded by northwest-trending contractional structures that are parallel to the regional physiographic boundaries, and perpendicular to the modern subduction direction of the Nazca plate (Figures 1 and 2). Key regional structures are the northeast-vergent Cusco-Lagunillas Fault to the southwest and the southwest-vergent Urcos-Ayaviri fault system to the northeast (Figure 1c). The most prominent local structure in the area is the northeast-vergent San Juan de Quihuares Fault, which appears to be a northern splay off the Acomayo Fault (Carlotto, 2013) (Figures 1c and 2).

Identification of formations in the field area and logging of a composite Cenozoic stratigraphic section was aided by previous mapping by the Instituto Geológico Minero y Metalúrgico (INGEMMET), and summary of previous basin research by Carlotto (2013). The Quilque Formation is the oldest Cenozoic strata in the region. Where measured, it is exposed conformably above overturned Upper Cretaceous strata (section 1 of Figure 2). Structural dip of Paleogene strata (the Quilque, Chilca, Kayra, Soncco, and Punacancha formations)

gradually changes up section from ~70° overturned to upright ~50°, and continues to decrease in dip angle to ~40° (sections 2–4 of Figure 2). The Punacancha Formation is truncated by the San Juan de Quihuares Fault (Figures 1c and 2). The regionally-limited and discontinuous Miocene Paruro Formation outcrops in the core of the larger Yaurisque syncline (Figure 1c), sitting in angular unconformity above the Kayra, Soncco, and Punacancha formations (section 5 of Figure 2), and bounded by the Acomayo Fault to the southwest (Figures 1c and 2) (Carlotto, 2013).

### 3. SEDIMENTOLOGY AND STRATIGRAPHY

#### 3.1. Methods

##### 3.1.1. *Lithofacies identification and associations*

Stratigraphic formations were measured in the field at decimeter resolution with a standard 1.5 m Jacob's staff using a modified lithofacies classification scheme from Miall (2010) in Dalrymple and James (2010), originally modified from Miall (1977). This classification scheme facilitates interpretation of depositional process by characterizing beds based on primary depositional features: bedding thickness, grain size, texture, and sedimentary structures. Eleven different lithofacies were identified, and are labeled in the detailed composite stratigraphic section in Figure 3.

Lithofacies codes are summarized in Table 1. Siltstones and limited claystones (Fm, Fl, and c) are interpreted to form from suspension settling; massive mudstones may also result from bioturbation (Figure 4a). Sandstones are classified as massive (Sm), ripple- or trough-cross-stratified, (Sr, St), and horizontally-laminated (Sh) (Figures 4b-d). Sm is typical of rapid deposition with limited stable bedform development, or potentially massive due to sediment reworking and redistribution from bioturbation. Ripple- and trough-cross-stratified sandstones (Sr and St) form from ripple and dune migration under unidirectional, lower-flow

regime flow conditions, whereas horizontally-laminated sandstones (Sh) form in supercritical, upper-flow regime plane-bed flow conditions with relatively high velocity (60 –  $\geq$  120 cm/s, depending on grain size) and/or in shallow water (e.g., Bridge & Best, 1988).

Massive matrix- and clast-supported conglomerates (Gmm and Gcm) are indicative of hyperconcentrated, plastic (high strength) debris flows and pseudoplastic pressure- or buoyancy-modified deposition, respectively (Figure 4e). Clast-supported imbricated conglomerates (Gcmi) indicate traction transport of migrating subaqueous barforms under unidirectional flow conditions, whereas similar deposits with crude horizontal bedding (Gch) also suggest traction transport, but resulting from deposition of subaqueous bars, gravel sheets, or gravel lag deposits (Figure 4f).

Lithofacies codes were grouped into five lithofacies associations to aid interpretation of depositional environments. Associations are similar to those presented in Perez and Horton (2014) and Horton et al. (2015), as their study areas along strike to the south (Figure 1c) share many similar stratigraphic characteristics, and to Altiplano strata in general (e.g., Hampton & Horton, 2007).

Lithofacies association F1 consists of thick (1–10s of m) packages of mudstones (Fm and Fl) with thinly interbedded (1–10s of cm) very-fine to fine-grain, tabular, often fining-upward, solitary beds or stacked bed sets (Campbell, 1967) of Sm, Sr, and Sh sandstones. F1 packages are interpreted as overbank deposition in a fluvial floodplain depositional environment (Figure 5a).

Lithofacies association S1 comprises thick (1–10s of m), tabular sandstone sheets dominated by Sm and Sh bodies with limited St, as well as rare, thin (1–10s of cm) interbedded Fm and Fl beds. Beds included in lithofacies association S1 have limited basal erosion or scour. We interpret lithofacies association S1 as the product of sand sheet

deposition in a broad unconfined fluvial system, similar to sand sheets documented elsewhere in the Bolivian Altiplano (Hampton & Horton, 2007) (Figure 5b).

Lithofacies association S2 contains St, Sh, and Sm bodies with limited mudstone interbeds. The key difference between S1 and S2 is the presence of significant basal scour and erosive channel forms (Figure 5c); these associations are similar in that they both form thick, laterally continuous, often amalgamated sandstone units that in many cases extend for multiple km, likely from deposition in a broad, braided fluvial depositional environment (Figure 5d).

Associations G1 and G2 both have Gmm and Gcm. The main difference is that G1 shows little to no basal scour that is characteristic of hyperconcentrated debris flows in an alluvial fan setting (Figures 4e and 5e), whereas G2 has basal scour, is in some places lenticular, crudely horizontally bedded (Gch), or imbricated (Gcni, Gchi), all of which are indicative of deposition of subaqueous gravelly bars, side bars, or channel fills in a braided fluvial or alluvial fan setting.

### ***3.1.2. Paleocurrent analysis and conglomerate clast counting***

Paleocurrent measurements were taken from preserved ripple bedforms, trough-cross-stratified sandstones, clast-supported imbricated conglomerates, primary-current lineations (parting lineations), and limited flute casts. Measurement of trough cross-bedding and calculation of paleoflow direction follows methods outlined in DeCelles et al. (1983). All measurements were corrected for deformational tilt using Rick Allmendinger's Stereonet 7 (Allmendinger, 2005).

Gravel clasts in conglomeratic units were counted in a roughly 100 x 100 cm area (minimum 100 clasts at each station). Clasts were divided into five different rock types: quartzite/metasedimentary, siliciclastic, volcanic, plutonic, and carbonate.

### **3.1.3. Sandstone petrography**

Sandstone petrography involves statistical assessment of framework grains (quartz, feldspar, and lithic fragments) through identification of their modal abundances. In addition to erodibility, resistance to chemical weathering, and a variety of other factors, framework grain modal abundance has been shown to be a function of provenance type that is in part governed by the tectonic setting during the timing of erosion (Dickinson & Suczek, 1979). Petrographic thin sections were made from fine- to coarse-grain sandstones, and stained for plagioclase and potassium feldspar to facilitate grain identification. Four-hundred sand-sized grains were counted in 37 sandstone samples following the Gazzi-Dickinson method of point counting (Table 2; Gazzi, 1966; Dickinson & Suczek, 1979).

## **3.2. Results**

Six Cenozoic formations were identified in the field and measured: the Quilque, Chilca, Kayra, Soncco, Punacancha, and Paruro formations. Formation descriptions presented below are organized from oldest to youngest, and grouped where similar. Results are shown in Figure 3 and summarized in Figure 6.

### **3.2.1. Quilque and Chilca formations**

The Quilque and Chilca formations represent the oldest Cenozoic strata in the region and have limited exposure in the Cusco area. These formations are relatively thin compared to younger Cenozoic formations, composing only ~600 of the ~6200 m of measured stratigraphic section. These characteristically dark red units represent an extensive period of low sediment accumulation.

The Quilque Formation is a ~400 m thick coarsening-upward succession sitting disconformably above the Upper Cretaceous siliciclastic and terrestrial carbonate Puquín Formation (Figure 6a). Basal mudstones contain abundant 0.1–0.3 mm diameter charophyte

fossils (terrestrial algae), identified as *Nitellopsis supraplana sulcate* (based on visual comparison to Antoine et al. (2016)), which suggests a Paleocene–early Eocene stratigraphic age (Mourier et al., 1988). This is consistent with previous interpretations of Paleocene age also based on charophyte fossils (*Lamprothamnium*, Carlotto, 1998), and a new detrital zircon U-Pb maximum depositional age of  $57.9 \pm 5.5$  Ma (see Section 4). The Quilque Formation comprises calcareous-cemented mudstones and rare fissile shales, paleosols, and marls at its base, and abruptly transitions to thick packages of calcareous-cemented dark red mudstones (F1) and tabular beds of very-fine- to fine-grain, feldspar-rich, calcareous-cemented sandstones (dominantly S1 with minor S2). Rare preservation of trough cross-bedding and primary current lineations shows northeast-directed paleoflow. Conglomerate compositions are dominantly quartzite (Figure 6). Sandstone compositions decrease in quartz up section, and have roughly equal proportions of feldspar and lithic fragments, with a greater proportion of volcanic lithics than sedimentary lithics (Figures 6c-d).

The Chilca Formation is a ~200 m thick coarsening-upward package of dark red mudstones and sandstones. The contact between the Quilque and Chilca formations has been previously documented as regionally disconformable (Carlotto, 2013); however, this relationship was not observed in the field due to poor exposure of these fine-grain units. Bedding geometry and sedimentary structures are similar to the upper Quilque with tabular S1 sandstones interbedded within thick packages of F1 mudstones. The Chilca overall has more F1 than S1 intervals compared to the underlying Quilque Formation. Limited St shows northeast-directed paleoflow. Sandstone composition is similar to the Quilque Formation, but with a slight increase in quartz (Figure 6).

### **3.2.2. Kayra and Soncco formations (San Jerónimo Group)**

The Kayra and Soncco formations together make up the San Jerónimo Group, which represents ~2800 m of the measured stratigraphic section as 500–1000 m thick coarsening-

upward packages of dominantly S1 sandstones and F1 mudstones. Sandstone packages in this group are distinct and pervasive in the region as they make up thick (10s of m), laterally-continuous (many km), tabular sandstone sheets in and around the study area (Figure 5d).

The Kayra formation is ~1200 thick and sits conformably above the Chilca Formation. A new detrital zircon U-Pb maximum depositional age places the base of the Kayra Formation at  $41.1 \pm 2.3$  Ma (see Section 4); this is slightly younger than a previously reported 53–46 Ma age (Carlotto, 1998; Carlotto et al., 2005, 2011). The lower Kayra Formation comprises thick packages of F1 mudstones with laterally continuous beds of non-erosive S1 and minor S2 that gives way to G2 and minor G1 conglomerates. The upper Kayra is dominated by S1 sandstones with minor F1 and S2 calcareous-cemented mudstones and sandstones. Sandstones in the upper Kayra contain an overall increase in S2, as well as abundant mud rip-up clasts, small fragments of charcoal, and plant material. Exposures of the Kayra Formation southwest of Cusco (outside the main study area) show predominantly north-northeast paleoflow (Carlotto, 1998, 2013). Conglomerate clasts in the lower Kayra are dominated by quartzite, with subordinate siliciclastic, carbonate, and volcanic clasts. The upper Kayra conglomerates are also dominated by quartzites, but with an increase in carbonate and volcanic clasts (Figures 3 and 6b). Sandstone compositions show a slight decrease in quartz and concomitant increase in feldspar (dominantly plagioclase) (Figure 6c and Table 3). Relative proportions of sedimentary lithics decrease up section compared to volcanic lithics (Figure 6d).

The Soncco Formation is ~1600 m thick with two distinct coarsening-upward successions (Figures 3 and 6a). The age of the basal Soncco was previously reported at 44–42 Ma (Carlotto, 1998; Carlotto et al., 2005); however, a new detrital zircon U-Pb maximum depositional age places the base of the Soncco slightly younger at  $36.5 \pm 3.2$  Ma (see Section 4). The lower Soncco Formation marks an abrupt transition from the sandstone-dominated

upper Kayra to ~800 m of dark red F1 mudstone deposition. This mudstone-dominated interval contains pervasive burrowing. As the formation coarsens up section, there is an increase in S1 sandstone deposition with abundant, large (up to 20 cm diameter) mud rip-up clasts. Volcaniclastic input and large (0.1–0.5 mm) plagioclase crystals increase in the upper Soncco Formation. The uppermost Soncco Formation, just below the transition to the Punacancha Formation, contains large reworked pebble-size volcanic fragments in medium- to coarse-grain sandstones; however, no volcanic tuffs were found in either formation (cf., Carlotto, 2013). Paleocurrent indicators show east- and northeast-directed paleoflow. Sandstone petrography reveals an increase in plagioclase compared to quartz and lithic fragments (Figures 6c-d), and interestingly, an increase in accessory minerals such as amphiboles and clinopyroxenes.

### **3.2.3. *Punacancha Formation***

The Punacancha Formation is ~1400 m thick and comprises multiple coarsening-upward successions (Figures 3 and 6a). New zircon U-Pb maximum depositional ages for the base and top of the section bracket deposition between  $27.4 \pm 2.4$  Ma and  $23.1 \pm 2.9$  Ma (see section 4); the basal age is similar to that previously reported by Carlotto et al. (2011) of ~30 Ma. The lower Punacancha Formation primarily comprises thick F1 mudstone and S1 sandstone beds. The upper Punacancha Formation comprises S1 and S2 sandstones with thick discontinuous packages of G1 and lenticular G2 conglomerates. The majority of the sandstone beds are Sm, with limited Sh and St. Although variable from north- to southeast-directed, paleocurrent measurements from the Punacancha Formation generally show northeast-directed paleoflow, consistent with previous measurements by Chavez et al. (1994). Conglomerate clast counts show varying proportions of quartzite, siliciclastics, volcanic, and plutonic clasts with limited carbonate clasts (Figure 6b). Despite the changes in lithofaces and

stratigraphic architecture, sandstone compositions are remarkably similar to that of the upper Soncco Formation.

#### **3.2.4. Paruro Formation**

The Paruro Formation is ~1400 m thick and sits in angular unconformity above the Kayra, Soncco, and Punacancha formations. The Paruro Formation has a basal age previously documented at  $10.1 \pm 1.1$  Ma based on K/Ar dating of a basal tuff, as well as Miocene age charophyte fossils (*Chara* and *Rhabdochara*) (Carlotto, 1998). New detrital zircon U-Pb geochronology maximum depositional ages place the base and top of the section at  $9.0 \pm 0.5$  Ma and  $7.4 \pm 0.8$  Ma (see Section 4). The formation is dominated by thick packages of S2 sandstone and G2 conglomerate beds. Covered intervals are typically a mix of F1 mudstones and friable S2 coarse-grain sandstones. Paleocurrent measurements show northeast-directed paleoflow. Conglomerate clast compositions are similar to those of the underlying Punacancha Formation, but show a continued increase in siliciclastic clasts and decrease in quartzite and volcanic clasts (Figure 6b). Sandstone compositions show a dramatic increase in quartz at the base of the section, followed by a return to plagioclase- and lithic-fragment-dominated compositions (Figure 6c), and an increase in sedimentary lithics up section (Figure 6d).

### **3.3. Summary and interpretation**

The Paleocene–early Eocene Quilque and Chilca formations reflect the end of Cretaceous carbonate deposition and the beginning of clastic infilling of the Altiplano basin in this region. This change in depositional environment is indicative of a larger regional transition from carbonate to siliciclastic deposition for the remainder of the Cenozoic. Basal Quilque deposition marks this change in depositional environment from low energy, fresh water (or brackish) lacustrine, as indicated by abundant charophyte fossils, to a fluvial

depositional environment. Northeast-directed paleocurrent measurements and quartzite-dominated conglomerates indicate sediment sourcing from the Western Cordillera and/or western Altiplano to the southwest, as quartzite formations are pervasive in those regions.

The Chilca formation is essentially a continuation of the upper Quilque Formation with deposition in a predominantly fluvial floodplain environment, but with a slight decrease in fluvial energy.

The Eocene Kayra and Soncco formations (San Jerónimo Group) show a drastic increase in stratal thickness as broadly coarsening-upward packages, and an overall increase in sandstone-to-mudstone ratio. The depositional environment near the base of this group is interpreted as fluvial floodplain with brief episodes of fluvial braid plain deposition, which transitions up section to extensive periods of unconfined sand-sheet deposition in a broad, wide fluvial system. These formations reflect an increase in fluvial energy, sediment supply, and accommodation, as they total nearly 3 km of the composite stratigraphic section.

Paleocurrent indicators are consistent with sediments sourced from the west and southwest; conglomerate clast counts from the Kayra Formation support this interpretation, as quartzite-dominated formations abound in the Western Cordillera and Altiplano physiographic regions.

Collectively, these interpretations point to deposition in a basin undergoing accelerating subsidence with an increasingly proximal Western Cordilleran and/or western Altiplano sediment source. Contrasting with previous interpretations, we did not find field evidence for shortening-related progressive unconformity development during San Jerónimo deposition (cf., Carlotto, 2013). Sandstone petrography supports this interpretation, as the increased presence of accessory minerals such as euhedral hornblendes and clinopyroxenes is characteristic of primary volcanic input with short transport distances, and indicative of increased proximity of the Western Cordilleran volcanic arc.

The Oligocene–upper Miocene Punacancha and Paruro formations represent some of the final stages of siliciclastic infilling of this part of the greater Altiplano. They also record a change from fluvial-dominated to alluvial fan-dominated depositional environment. The Punacancha Formation represents a coalescing of alluvial fans (bajada) pouring sediment off the immediately-adjacent retroarc fold-and-thrust belt of the Western Cordillera. Variable paleocurrent measurements to the north and southeast support this interpretation, as the retroarc fold-and-thrust belt front would have likely had a northwest-southeast oriented strike. The increase in plutonic clasts in conglomerates is consistent with exhumation and erosion of the 48–32 Ma Andahuaylas-Yauri batholith (Figure 1c) consisting of earlier gabbro–diorite compositions later intruded by granodiorites and quartz monzodiorites (Perelló et al., 2003). Above the angular unconformity that separates these formations, sandstone compositions change from dominantly quartz at the base of the formation, then steadily return to dominantly plagioclase, which is consistent with tapping of a new sediment source (likely quartzite based on dominance of Qp) followed by renewed sediment sourcing of the Western Cordillera and western Altiplano.

## 4. DETRITAL ZIRCON

### 4.1. Methods

#### 4.1.1. *U-Pb geochronology*

Detrital zircon U-Pb geochronology, a well-established analytical tool for assessing sediment provenance and maximum depositional age (e.g., Gehrels, 2014), was conducted at the University of Houston (see Supplementary Material S1 for detrital zircon U-Pb procedures, analysis, and data reduction; Košler et al., 2002; Paces & Miller, 1993; Shaulis et al., 2010; Sláma et al., 2008; Stacey & Kramers, 1975). Sandstone samples were collected from the Quilque, Kayra, Soncco, Punacancha, and Paruro formations. A pumice-rich

reworked tuff was also collected from the base of the Paruro Formation. Potential sediment source samples were collected from the quartzite-dominated Jurassic–Cretaceous Puente, Labra, Hualhuani, and Huancané formations, which have not been previously characterized in the region. These potential source samples were compiled with previously published Paleozoic–Mesozoic detrital zircon U-Pb data from sandstones for comparison to Cenozoic basin samples (summarized in Table 4).

The youngest detrital zircon U-Pb age or age population in a detrital sample is a measure of the maximum depositional age of the sample stratum, and can provide important chronology in siliciclastic strata lacking alternative methods of age control. Recent work along strike to the south near Ayaviri (Figure 1c) has shown maximum depositional ages in this region closely approximate true depositional age due to ongoing volcanic input throughout the Cenozoic (Perez & Horton, 2014). Given the likelihood of approximating true age of the strata in this type of tectonic setting (Cawood et al., 2012), maximum depositional ages were used to calculate sediment accumulation rates for comparison to previously documented Andean plateau foreland basin stratigraphy to the south.

#### ***4.1.2. Multidimensional scaling (MDS)***

Multidimensional scaling (MDS) is a superset of principal component analysis that has recently been adapted for comparison of detrital data sets (Vermeesch, 2013), and shown to facilitate comparison of multiple detrital data sets (e.g., Che & Li, 2013). Metric MDS (cf., non-metric MDS) produces Cartesian plots in N dimensions through conversion of sample dissimilarity to disparity via linear transformation and iterative rearrangement of data in Cartesian space, seeking to minimize the misfit between intersample distance and disparity (termed “stress”). A low stress level indicates a reasonable transformation, and a correlation between sample dissimilarity and distance, resulting in similar samples clustering closer together in Cartesian space. Metric MDS is applied by first constructing a pairwise

dissimilarity matrix of detrital age distributions. One such metric used to calculate dissimilarity between detrital samples is the two-sample Kolmogorov-Smirnov (KS) statistic D value (the maximum distance between two empirical cumulative distribution functions, CDFs) (Stephens, 1970; Vermeesch, 2013). Because the KS test is more sensitive about the median, and does not take into account sample uncertainty, we constructed a dissimilarity matrix using the coefficient of non-determination ( $1-R^2$ ), where  $R^2$  is the Cross-correlation coefficient calculated from cross plots of sample probability density. This quantitative measure of similarity is more sensitive than the KS test D value both for the number of age modes in a detrital age distribution, as well as the relative proportions of those modes (Saylor et al., 2013; Saylor & Sundell, 2016). We applied this method using the program DZmds from Saylor et al. (2017).

#### ***4.1.3. Mixture modeling***

Mixture modeling of detrital zircon U-Pb data was used to determine the contributions of individual sediment sources by randomly mixing potential source age distribution probability density plots for comparison to basin samples. The mixing model employed here, DZmix (Sundell & Saylor, 2017), determines a range of best mixtures of potential sources using an inverse Monte Carlo approach of randomly scaling each source age distribution by a random set of percent contributions that sum to 100%, summing the scaled distributions to give a single model distribution, and quantitatively comparing that model distribution to a basin sample distribution through Cross-correlation. This process is repeated 100,000 times for each basin sample, and the best 100 model fits (0.1%) are used to calculate the mean and standard deviation ( $1\sigma$ ) contribution from each potential source. All potential sediment sources used in the mixing model are considered equally likely contributors to Cenozoic Altiplano strata because we do not know (and cannot know) *a priori* what was exposed and being eroded during the timing of deposition, as much of the Andean plateau is mantled with

Neogene volcanic rocks. The model is capable of determining non-contributing sources (i.e., 0% contribution to the basin). Source distributions have few ages younger than 200 Ma (8 out of 2,693), and therefore only ages older than 200 Ma were considered in the mixture modeling. Results are therefore minimum estimates for sediments sourced from the Western Cordillera, as all Cenozoic Altiplano samples contain abundant detrital populations < 200 Ma that are unaccounted for in the model results.

#### **4.1.4. Roundness**

Zircon roundness has been previously used as a proxy for sediment transport distance and sediment recycling (e.g., Decou et al., 2013). Roundness was calculated for zircon grains with concordant U-Pb age dates. To quantify zircon roundness, we developed a MATLAB-based code to employ the roundness quantification method outlined in Diepenbroek et al. (1992). This method uses the relationship between the centroid of a grain and the distance from the centroid to its perimeter based on two-dimensional images of individual zircon grains. The MATLAB code calculates roundness in the following steps: 1) Each image is converted into a binary matrix of ones and zeros, 2) the perimeter and centroid of the grain is determined and converted from Cartesian to polar coordinates to measure the magnitude of the ray ( $\rho$ ) from the reference point (origin/centroid) to perimeter for  $\theta$  angles of 0 to 359°, 3) harmonics are calculated using a fast Fourier transform of a  $\theta$ - $\rho$  x-y plot, 4) harmonics are normalized to the 0th Fourier coefficient (which removes any grain size effects) and the first harmonic is removed (which removes the aspect ratio effect), and finally 5) the 2nd–24th harmonics are summed and scaled to maximize the sensitivity between 0 and 1. We benchmarked our code to results in Diepenbroek et al. (1992) using the Krumbein (1941) roundness table, as was done in the original Diepenbroek et al. study. Because detrital zircons vary considerably in size and shape, especially in aspect ratio, we tested the code on synthetic data (drafted zircon images of different sizes and shapes) to verify its utility for zircon. We

found the method of Diepenbroek et al. (1992) gave the more consistent results for zircons compared to alternative roundness quantification methods (e.g., Takashimizu & Iiyoshi, 2016).

## 4.2. Results

### 4.2.1. U-Pb geochronology

Nine samples from seven stratigraphic levels of Cenozoic Altiplano strata and five samples from four Jurassic–Cretaceous potential sediment source formations were analyzed (Figure 7). Results are reported with characteristic age groups shown as colored vertical bars to highlight potential sediment sources (discussed in Section 2.1). These age groups include arc volcanics (< 200 Ma), Permo-Triassic Mitu Group (200–300 Ma), Famatinian (400–500 Ma), Pampean-Braziliano (500–700 Ma), Sunsás-Grenville (900–1200 Ma), and cratonic (> 1500 Ma) (Figure 7d). Cenozoic Altiplano basin and Jurassic–Cretaceous potential source samples show similar proportions of each of these characteristic groups. Potential sediment source samples are combined with previously characterized potential source formations (see Table 4 and references therein). Older potential sediment source formations also show many of the same characteristic age groups (Figure 7a).

Results for maximum depositional ages for all but one sample are within  $2\sigma$  uncertainty of the mean and  $1\sigma$  propagated uncertainty of the youngest three grain ages, as recommended by Dickinson and Gehrels (2009). The exception is the base of the Paruro Formation: the youngest single-grain maximum depositional age is  $8.6 \pm 0.9$  Ma, but the mean and  $2\sigma$  uncertainty of the youngest three grains is  $19.9 \pm 3.7$  Ma. Fortunately, we also sampled a pumice-rich reworked tuff (sample 20140605-02) that gave a basal age date of  $9.0 \pm 0.5$  Ma (see Supplementary Material for details). This is within uncertainty of a previously

reported K/Ar age from a basal tuff of  $10.1 \pm 1.1$  Ma reported by Carlotto (2013). For all other samples the single youngest age was used to infer maximum depositional age.

Detrital zircon U-Pb maximum depositional ages bracket the timing of deposition for the ~6200 m of measured strata between ~58 and ~7 Ma. (Figures 6a and 7a). Best estimates for sediment accumulation rates calculated based on stratigraphic thickness and single-grain maximum depositional ages give 36 m/Myr during Quilque and Chilca deposition, 261 m/Myr during Kayra deposition, 175 m/Myr during Soncco deposition, 333 m/Myr during Punacancha deposition, and 875 m/Myr during Paruro deposition. A basal age of 10.1 Ma for the Paruro Formation from Carlotto (2013) gives a rate of ~520 m/Myr.

Visual comparison of Cenozoic Altiplano probability density plots is difficult because they show very similar proportions of the characteristic age groups typically found in detrital zircon U-Pb age distributions from southern Peru (e.g., Bahlburg et al., 2009, 2011; Reimann et al., 2010; Perez & Horton, 2014). Integration of probability density plots based on characteristic source age ranges plotted against maximum depositional age aids first-order up-section comparison of these data (Figure 7b). Results show Cenozoic arc volcanic ages occur in high percentages (30–70%) in the lower Kayra (~41 Ma), upper Punacancha (~23 Ma), and upper Paruro (~7 Ma) formations, and are relatively low (10–25%) in the Quilque, Soncco, and lower Paruro Formations. In contrast, Mesozoic-aged zircons steadily decrease from 20–30% in the lower sections to < 10% at the top. A second set of integrations shown in Figure 7b (right) with ages < 200 Ma removed helps to identify potential provenance signatures obscured by pervasive volcanism throughout the middle Cretaceous–Cenozoic. Permo-Triassic Mitu and Famatinian source ages represent < 15% source contribution throughout the section. Pampean-Braziliano ages consistently make up 20–30% with higher percentages in the Quilque and Kayra formations. Sunsás-Grenville ages make up 15–30%, with the highest proportions in the Soncco and upper Paruro formations. Cratonic signatures

compose roughly 10–20% of Altiplano age distributions, with the lowest proportions at the bottom and top of the measured strata.

#### ***4.2.2. Multidimensional scaling (MDS)***

Detrital zircon samples from Cenozoic Altiplano strata were compared to each other and to fourteen potential source samples (Figure 8a) using three-dimensional (3D) MDS (Figure 9). The pairwise dissimilarity matrix used to construct MDS plots shown in Figure 8b is color-coded to distinguish more and less similar age distributions. Transformation from dissimilarity to distance and disparity in 3D gives a good correlation as shown by a low stress (0.1147, Figure 9a). Results show Altiplano basin samples are most similar to each other and to Jurassic–Cretaceous source samples (Figures 8b and 9b-d). Paleozoic source samples are the most dissimilar, as shown by greater distances from the cluster of Altiplano samples.

Although the Calapuja Formation is far from the cluster of Altiplano basin samples, its nearest neighbor (black arrows in Figures 9b-d) is the Soncco Formation, implying high similarity and a good candidate as a sediment source at ~36 Ma.

#### ***4.2.3. Mixture modeling***

Mixture modeling results show zircon populations of late Jurassic–early Cretaceous formations make up 55–65% of the Cenozoic Altiplano age distributions < 200 Ma (Figure 10a). The remainder is a mixture of Permo-Triassic and older formations, with relatively large (25–30%) contributions from the Ordovician Calapuja Formation from 36–27, and at ~7 Ma. Source contributions from the Western Cordillera are dominantly from age distributions of the Hualhuani and Puente formations from 50–42 Ma, and the Puente Formation from 36–7 Ma (Figure 10a and Supplementary Material).

Mean Cross-correlation coefficients of the top 0.1% model fits indicate that the model can reproduce detrital age distributions for all Paleogene samples except the late Oligocene

(upper Punacancha). Mean Cross-correlation coefficients of  $> 0.7$  for this interval approach that for a perfect mixture model fit of  $R^2 = 1$ . This indicates that the sources are well-characterized, and that the selected source samples may indeed represent the true sources from which Paleogene strata were derived. However, the upper Punacancha and lower Paruro formations show poorer model fits (Figure 10b). This indicates that there may be a sediment source missing, that the basin and/or potential sources have not been adequately characterized, or both. It is worth noting these model results represent nonunique, best-fit solutions that are based on available source formation age distributions, and are testable with additional source sample and basin detrital geochronology.

#### **4.2.4. Roundness**

Zircon roundness results plotted against U-Pb maximum depositional age show a decrease in roundness from  $\sim 58$  to  $\sim 27$  Ma for combined samples (Figure 11A), and for samples divided into characteristic sediment source age groups based on their U-Pb ages (Figure 11b). In both cases, zircons become more round in the late Miocene, and do not return to the level of roundness shown in the Paleocene. Detailed results of roundness calculations and uncertainties are available in the Supplementary Material.

Application of the Student's t-test to zircon roundness versus age confirms that the observed roundness trends are statistically robust. The t-test tests the null hypothesis that two independent samples come from distributions with equal mean values based on their standard deviations (Hazewinkel, 2001). For roundness results using all grains from each sample (Figure 11a), 80% of mean values are statistically different from one another at the 95% confidence level; all samples are different at the 90% confidence level. The base of the Quilque, Punacancha, and Paruro samples (i.e., comparison of the oldest and youngest of our interpreted foreland basin samples, and an interpreted hinterland basin sample) are statistically different from one another at the 95% confidence level. Roundness results

subdivided into characteristic source populations (Figure 11b) are less statistically robust: 52% of results have statistically different means from one another at the 95% confidence level; 72% are different at the 70% confidence level. The base of the Quilque is statistically different from the Paruro for all subpopulations of ages at the 95% confidence level except for Famatinian age zircons where it is different at the 90% confidence level. Punacancha zircons are not statistically different from Paruro zircons when divided into individual subpopulations.

#### **4.3. Summary and interpretation**

Results from detrital zircon U-Pb geochronology and quantitative provenance methods are consistent among themselves and to sedimentology and stratigraphy results presented in Section 3, indicating dominant sediment sourcing from the Western Cordillera and western Altiplano throughout the Cenozoic. Mixing model results are consistent with a conceptual unroofing sequence of Mesozoic sediment sources. Initial unroofing of the Lower Cretaceous Hualhuani Formation in the Paleocene–early Eocene is followed by erosion of the Jurassic Puente and Ordovician Calapuja formations from 36–7 Ma (Figure 10a). Assuming that introduction of new sediment sources can be linked to crustal deformation, pulses of Calapuja sediment sourcing are interpreted to correspond to periods of contractional deformation where hanging wall thrust blocks expose and recycle underlying Ordovician strata to the west, or along the Eastern Cordilleran backthrust belt at ~36 and ~7 Ma (Figure 10a). We favor deformation to the west or southwest (i.e., Western Cordillera or western Altiplano) throughout this interval because sources identified through mixture modeling outcrop exclusively in these areas. Mixture of sources from the Eastern Cordillera results in a poorer fit to our measured basin samples than those from the west. Although recent work suggests zircon roundness is not easily connected to transport distance (Muhlbauer et al., 2017), we observe a statistically robust up-section decrease in zircon roundness in Paleogene

strata that is independent of sediment source or zircon age group. We attribute decreased zircon roundness to a decrease in fluvial transport distance, as this is consistent with thrust-belt advance and encroachment of Western Cordilleran sediment sources toward the study area between ~58 and ~27 Ma. Interestingly, this decrease in roundness is seen in recycled sediment sources that make up the majority of ages  $> 200$  Ma, as well as ages  $< 200$  Ma that are most likely derived from Mesozoic–Cenozoic arc volcanism, which is consistent with zircon roundness being controlled by sediment transport distance.

## 5. DISCUSSION

### 5.1. Paleogene foreland basin development

Stratigraphy and sediment provenance results interpreted in the context of new age control provided by detrital zircon U-Pb maximum depositional ages points to Paleogene development of a flexural foreland basin system in the northernmost Peruvian Altiplano. Thick (100–500 m) coarsening-upward packages of siliciclastic strata in an overall coarsening-upward succession typifies this geodynamic setting (DeCelles, 2012). Low sediment-accumulation rates ( $< 50$  m/Myr) from 58–41 Ma, followed by rates  $> 150$  m/Myr from 41–23 Ma are consistent with initial deposition of distal foredeep mudstones and fine-grain sandstones transitioning to more proximal foredeep deposition of thick packages of sandstones and conglomerates (DeCelles & Giles, 1996; Xie & Heller, 2009; DeCelles, 2012; Allen & Allen, 2013) (Figure 12). Paleogene paleocurrent measurements consistently show northeast-directed paleoflow from highlands to the southwest (i.e., the Western Cordillera). Conglomerate clast counts show a decrease in quartzite and increase in plutonic and sedimentary clasts which may be interpreted as initial sourcing of ubiquitous Mesozoic quartzites in the Western Cordillera followed by tapping of the deeper, locally-intruded Eocene–Oligocene plutonic rocks of the Andahuaylas-Yauri batholith along the northeastern boundary of the Western Cordillera (Figure 1c). Sandstone compositions consistently contain

abundant volcanic fragments and plagioclase feldspar with an overall decrease in monocrystalline and polycrystalline quartz throughout the Paleogene, further suggesting consistent sediment sourcing from the Western Cordilleran volcanic arc. Sediment provenance information from detrital zircon quantitative methods (MDS and mixture modeling) supports this interpretation, as Cenozoic Altiplano age distributions are more similar to Mesozoic source formations prevalent in the Western Cordillera and western Altiplano than to Paleozoic strata to the east (Figures 9 and 10) and Mesozoic–Cenozoic zircons ages characteristic of the Western Cordillera are ubiquitous in Cenozoic Altiplano basin samples. Detrital zircons decrease in roundness through the Paleogene for all characteristic sediment source age groups, including those interpreted to be sourced from arc volcanics (Figure 11). Decreased roundness interpreted as less sediment transport distance is consistent with increasing proximity of the Western Cordillera in the Paleogene as it migrated toward the modern study area (Figures 11 and 12).

Increased sediment input and accommodation along with continued sediment sourcing from formations from the west and southwest is consistent with flexural subsidence induced by increasing proximity and loading by the Western Cordillera in the Paleogene (Figure 12). Alternative Paleogene subsidence mechanisms such as strike-slip, extensional, thermal, and dynamic subsidence processes are not supported by observations in the region (see discussion in Horton et al., 2015). However, these results do not necessarily preclude an early Paleogene load in the Eastern Cordillera (e.g., Gotberg et al., 2010; Rak et al., 2017). Modern crustal thickness variations in the Andean plateau are consistent with Airy isostatic support (Beck et al., 1996). Modern departure from Airy isostacy along the eastern edge of the Andean plateau is interpreted from a breakdown in the expected inverse correlation between topography and Bouguer gravity anomalies (Horton & DeCelles, 1997). This was likely also the case in the

Paleogene, with a change from Airy isostatic to flexural support from the topographic high of the orogenic wedge to the leading eastern edge, similar to the modern Subandes.

## 5.2. Neogene hinterland basin deposition

The Neogene Paruro Formation represents renewed deposition following deformation, uplift, and denudation as propagation of the retroarc thrust front deformed and consumed earlier foreland basin deposits before ultimately merging with the developing Eastern Cordillera (Figure 12). Remnant wedge-top deposits are preserved as the Anta Formation (age equivalent strata to the Soncco Formation) to the west and southwest along the northeastern boundary of the modern Western Cordillera (Carlotto, 2013) (Figure 1c). Sandstone petrography reveals a major increase in mono- and polycrystalline quartz at the base of the Paruro Formation before returning to compositions similar to those in the Paleogene (Figures 6c and 6d), which when combined with mixing model results may be interpreted as increased sediment input from shortening-related exposure of Ordovician–Devonian stratigraphic formations (Figure 10). The timing of hinterland basin deposition in the Cusco region is younger than has been documented along strike to the south in the Ayaviri Basin, which occurred as early as 29 and 26 Ma based on well-dated growth strata in the footwall of the Eastern Cordillera backthrust belt (Perez & Horton, 2014; Horton et al., 2015).

Results from sediment composition and detrital zircon U-Pb mixture modeling, when combined with consistently north-northeast-directed paleocurrents, points to shortening-related deformation to the west and southwest of the study area. Candidate structures along the boundary of, and within the modern western Altiplano are the east-vergent Cusco-Lagunillas and/or Pasani-Acomayo regional fault systems (Figures 1c and 2). The 23–9 Ma angular unconformity brackets local Neogene deformation. Candidate structures based on cross-cutting relationships are the east-vergent Acomayo and/or San Juan de Quihuares thrust

faults. This timing of shortening is consistent with the Pasani fault (Figure 1c) to the southeast which currently bounds the Ayaviri basin, interpreted to be most recently active from 18–16 Ma (Perez & Horton, 2014). The Acomayo fault and/or San Juan de Quihuares faults may represent a northern continuation of the Pasani fault system in the Peruvian Altiplano, as it shares a similar vergence direction and crosscuts many of the same rock units (Figure 1c). If accurate, these structures may point to a regionally-connected system of deformation during the late stages of Andean plateau development.

Sediment accumulation rates of the Miocene Paruro Formation are very high ( $> 800$  m/Myr), and cover a short ( $< 3$  Myr) time interval (Figure 12). Such high rates and short deposition durations are characteristic of strike-slip subsidence (Xie & Heller, 2009; Allen & Allen, 2013). The Paruro Formation has been previously interpreted as a strike-slip basin (Carlotto, 2013), as have other structures in the Peruvian Andean plateau based on magmatism and inferred plate dynamics (e.g., Soler & Bonhomme, 1990). Where preserved, the basin has a high length-to-width ratio of ~9:1, which is on the upper end of typical elongate strike-slip basins (Nilsen & Sylvester, 1999). Invoking strike-slip faulting also implies vertical-axis rotations, which has been suggested to explain development of the Bolivian orocline from 25–12 Ma, with continued transpressional deformation post 12 Ma throughout the Peruvian Altiplano (Rousse et al., 2005; cf., Arriagada et al., 2003). Despite stratigraphic and provenance records pointing to a strike-slip subsidence mechanism, there is little supporting structural evidence (i.e., there are few mapped strike-slip faults in the area). This may be explained by overprinting of left-lateral transpressional structures by more dip-slip contraction, which is consistent with the changing plate convergence geometry in the middle to late Miocene from oblique to more orthogonal convergence (Pilger, 1984; Pardo-Casas & Molnar, 1987). If indeed stresses were previously more transpressional, the broad left step at the northern end of the Acomayo fault provides a subsidence mechanism, as a left

step in a left-lateral transtensional system would produce a releasing bend. Transpressional deformation may also produce local flexural subsidence in what Nilsen and Sylvester (1999) call “miniforeland-type basins” commonly adjacent to uplifted blocks in oblique-slip systems.

As in the modern, there was likely interplay of both flexural and isostatic support for the growing load of the nascent Andean plateau in the Paleogene. The crustal thickness in the modern Altiplano and adjacent Cordilleras is up to 60–70 km (Beck & Zandt, 2002), which cannot be supported by lithospheric flexure alone (Molnar & Lyon-Caen, 1988). The location of the modern forebulge east of the Andean plateau (Horton & DeCelles, 1997) further precludes complete flexural support in the modern Peruvian Altiplano. Hence, we envision the transition from foreland to hinterland basin deposition should be accompanied by a change from regional flexurally supported crust to locally isostatically supported crust.

### **5.3. Geodynamic implications: basin subsidence and surface uplift**

Peruvian Altiplano foreland basin stratigraphy highlights significant along-strike variability in the timing and location of foreland deposition of a regionally-contiguous Cenozoic foreland basin system that extended for hundreds of km along strike of the eastern Andean margin from southern Peru, through Bolivia, and into northwest Argentina (Horton et al., 2001, 2002, 2015; DeCelles & Horton, 2003; DeCelles et al., 2011; Carrapa et al., 2012) (Figure 13). The onset of high ( $> 100$  m/Myr) sediment accumulation rates occur earlier in the northern Andean plateau of southern Peru and northern Bolivia, and later in southern Bolivia and Argentina (Figure 13). This results in the thickest sections of foreland basin strata deposited during foredeep deposition in the north, and during wedge-top deposition in the south (Figure 13). In fact, most wedge-top deposits in the north are not preserved in the same locations as the foredeep deposits, or not preserved at all (Figure 13).

The trend of high sediment accumulation rates occurring later temporally, and later in terms of typical foreland basin system development (DeCelles & Giles, 1996) could result from two scenarios: 1) the trend is apparent, and the result of bias in the location of preserved and documented foreland deposits relative to the propagating orogenic wedge, or 2) the trend is real, and thus requires a geodynamic explanation for such a southward younging. To determine whether there is a difference in the onset of rapid sediment accumulation from north to south, the predicted migration of the Andean flexural wave may be compared to relative locations following the methods of DeCelles and DeCelles (2001). Here, flexural wave migration rate = shortening rate + rate of orogenic wedge widening. There is nearly 20 Myr difference in the onset of rapid ( $> 100$  m/Myr) sediment accumulation between the northern and southern locations. Long-term shortening rates in the Cenozoic central Andes are  $\sim 10$  mm/yr (Oncen et al., 2006). The DeCelles and DeCelles (2001) method gives a long-term wedge widening rate of  $\sim 8$  mm/yr, yielding a flexural wave migration rate of  $\sim 18$  mm/yr. Thus, a 20 Myr difference in the timing of onset of rapid sediment accumulation rate would require a  $\sim 360$  km difference in their locations for the flexural wave to pass between the sites. In this context, the relative location of these studies compared to the location of the modern orogenic front in the Subandes cannot account for the difference in the onset of rapid sediment accumulation, and there must be an explanation for the apparent trend involving the complex convergence history of the central Andes. A potential scenario involves inheritance of orogen-scale, antecedent structural and stratigraphic differences of the central Andes (McGroder et al., 2015), which may have caused Cenozoic foreland development to respond differently to along orogenic strike (discussed further below).

Development of a foreland basin system in the northern Peruvian Altiplano requires lithospheric loading of the Western Cordilleran hinterland and relative subsidence to the east in the location of the modern Eastern Cordillera. The former can be explained through

increased topography and proximity of the Paleogene Western Cordilleran magmatic arc and orogenic front to the study area (Mamani et al., 2008, 2010), as elevations were likely moderately high (1–2 km) before the middle Miocene (Saylor & Horton, 2014). However, the latter is in contrast to thermochronometric data from the Eastern Cordillera, which suggest pulses of exhumation and building of topography in the middle Eocene–late Oligocene (Gillis et al., 2006), and Eocene to late Miocene (Perez et al., 2016b), overlapping in time when foreland basin records predict relative subsidence.

There are similar conflicting lines of evidence between flexural-foreland-related basin subsidence interpreted from stratigraphic records and shortening-related exhumation interpreted from thermochronology in other parts of the central Andes. For example, foreland basin records in southern Bolivia reveal Oligocene (to possibly earliest Miocene) foredeep deposition (DeCelles & Horton, 2003) the same time and general location as Ege et al. (2007) interpret late Eocene–Oligocene exhumation and cooling (Figure 13). Further, foreland basin records in northwest Argentina require flexural subsidence and Eocene–Oligocene foredeep deposition (DeCelles et al., 2011) at the same time as Eocene–Oligocene shortening-related deformation interpreted from thermochronology (e.g., Deeken et al., 2006). Reconciling these conflicting lines of evidence between basin subsidence and thermochronometric records in the Andean Eastern Cordillera requires one of the following: 1) that the preserved stratigraphic succession discussed above does not represent a classically defined foreland basin system, 2) reinterpretation of existing thermochronology data, or 3) revision of our understanding of the geodynamics of foreland basins, perhaps with an alternative flexural model for foreland basin development capable of incorporating an Eastern Cordilleran load within the flexed lithospheric plate. DeCelles and Horton (2003) invoke a similar model for the latter in the Bolivian Andes, but do not explain in detail the geodynamics for such a

system. Reconciling these conflicting lines of evidence provides an avenue for future investigation.

#### 5.4. Foreland basin development and cyclical orogenic processes

Models of orogenic cyclicity for Cordilleran-type mountain belts have been used to explain records of mountain building in the context of predictable, cyclical geodynamic processes manifested as periods of high-flux magmatism, crustal thickening, and surface uplift (DeCelles et al., 2009, 2015). This model predicts that partial melting of underthrusted continental lower crust and mantle lithosphere drives periodicity in high-flux magmatism and emplacement of a high-density restitic and eclogitic crustal root during magma generation and lower crustal thickening. Development of a dense restite or eclogite keel is the result of internal deformation that results in regional elevation gain and building of wedge taper (*sensu* Davis et al., 1983). This takes place until a critical mass of the gravitationally-unstable crustal root founders via Rayleigh-Taylor instabilities (Göğüş & Pysklywec, 2008; Currie et al., 2015) or mantle-lithosphere delamination (Kay & Kay, 1993; Krystopowicz & Currie, 2013) into the underlying asthenosphere, ultimately resulting in a net elevation gain through isostatic adjustment, and accompanied by ignimbrite eruptions. Increased elevation places the orogen into a state of supercritical wedge taper that drives rapid foreland-directed propagation of the retroarc fold-and-thrust belt and concomitant migration of the foreland basin system. The cycle then begins anew, repeating in a 25–50 Myr time scale, with the rate of repetition of the cycle is dependent on, among other factors, the rate of simple-shear underthrusting of lower crust and lithospheric material (DeCelles et al., 2011).

The majority of observations in support of the orogenic cyclicity model come from southern Bolivia and northwest Argentina (e.g., Carrapa & DeCelles, 2015; DeCelles et al., 2015; Ducea et al., 2015), leaving southern Peru largely undiscussed in terms of cyclical processes. Despite this, many similar cyclical processes are observed in this region. There are

apparent pulses of magmatism based on combined bedrock ages from 13–18°S (from the Central Andes Geochemical and Geochronology Database, <http://andes.gzg.geo.uni-goettingen.de/>) and < 100 Ma detrital zircon U-Pb ages from Cenozoic Altiplano strata (Figure 14). Sediment accumulation rate dramatically increases during the interpreted high-flux event between 40 and 23 Ma, which coincides with an inboard step of widespread magmatism and deformation in southern Peru that has been linked to a period of flat-slab subduction, but without suppressing magmatic activity (Mamani et al., 2010) (Figure 14). Also, upward-coarsening packages tend to follow apparent pulses of magmatic activity (compare Figures 6a and 14). These latter two points suggest increased flexural loading may be linked to magmatic emplacement and crustal loading, which has been previously invoked to explain flexural subsidence of the lithosphere for other orogenic systems (e.g., Peterman & Sims, 1988). Sr/Y isotopic ratios from igneous bedrock samples, which have been shown to correlate with crustal thickness (Chapman et al., 2015; Profeta et al., 2015), display a stepwise increase at 40–30 Ma, and from 20 Ma to present. These steps coincide with widespread Paleogene magmatism (Mamani et al., 2010) and Neogene records (Saylor & Horton, 2014; Kar et al., 2016), respectively (Figure 14). Lithospheric foundering as expressed by periods of mantle-derived magmatic input with decreased  $^{143}\text{Nd}/^{144}\text{Nd}$  and elevated La/Yb and/or Sm/Y values (e.g., Kay et al., 1994; Haschke et al., 2002, 2006), has yet to be documented in southern Peru. Similarly, there are no records of Cenozoic hinterland extension, as observed in the Puna plateau (e.g., Schoenbohm & Strecker, 2009). Collectively, these observations tentatively support the orogenic cyclicity model in southern Peru, as defined by 80–60 and 45–20 Ma high-flux magmatic stages of the cordilleran cycle (Figure 14).

The timing of cyclicity in southern Peru and northwest Argentina are slightly out of phase. This is highlighted by the timing of high-flux events and intense magmatic activity in

northwest Argentina at 50–45 and 15–5 (DeCelles et al., 2015) (Figure 14). This southward offset in predicted phases of the model also tracks the apparent southward onset of rapid sedimentation (Figure 13). A key difference in the orogenic cyclicity model of DeCelles et al. (2015) and DeCelles et al. (2009) from other cyclicity models (e.g., Ramos, 2009; Ramos et al., 2014), is the role underthrusted continental material plays in driving cyclicity. Specifically, underthrusted continental lower crust and mantle lithosphere is more prone to melting and producing abnormally high fluxes of magma production and emplacement of dense restite and eclogite (Ducea & Barton, 2007), thus producing gravitational instability leading to foundering of the mantle lithosphere. The rate of upper plate lithospheric underthrusting is controlled by the geometry and basement involvement of the fold-and-thrust belt. Cenozoic contractional deformation on the eastern edge of the central Andes is at least in part controlled by preexisting Paleozoic and Mesozoic structural domains (McGroder et al., 2015). There is a distinct difference in inherited structures just south of the Bolivia–Argentina border where a transition from the Bolivian salient and in situ South American basement to lithosphere dominated by accreted terranes and antecedent Paleozoic structural fabrics (McGroder et al., 2015). This may control the north-to-south transition from dominantly thin-skinned fold-and-thrust belt contractional deformation in southern Peru to southern Bolivia to more basement-involved deformation in northwest Argentina during the Cenozoic, and the rate of lithospheric underthrusting. If the rate at which continental material is underthrust directly controls when and where high-flux events occur (thin- vs thick-skinned thrusting being faster and slower, respectively), then the preexisting structural fabric of the Paleozoic–Mesozoic central Andes may explain the apparent out-of-phase cycles observed between southern Peru and northwest Argentina. Alternative processes such as north-south migration of flat slab subduction (Ramos and Folguera, 2009), differences in rate and location of densification of mantle lithosphere (e.g., Garzione et al., 2008), or ductile crustal

flow (e.g., Gotberg et al., 2010; Garzione et al. 2017) may have also played a role in the apparent differences in cyclicity along orogenic strike.

## 7. CONCLUSIONS

We document ~6200 m of Cenozoic non-marine siliciclastic strata and new depositional chronology based on detrital zircon U-Pb maximum depositional ages in the northern Altiplano of southern Peru that documents the development and passage of a foreland basin system. Foredeep deposition occurs from 41–23 Ma, as evidenced by high (>150 m/Myr) sediment accumulation rates. Rapid (> 800 m/Myr) Miocene hinterland deposition of the Paruro Formation may reflect strike-slip subsidence related to regional transpression. Sediment provenance indicators consistently point to western-sourced sediments from the Cenozoic Western Cordillera and western Altiplano throughout the Paleogene. Results suggest there was a regionally-contiguous Paleogene foreland basin system on the eastern edge of the Andes for hundreds of km along strike. Development of a foreland basin system requires Paleogene lithospheric loading of the Western Cordilleran hinterland and relative flexural subsidence to the east in the location of the modern Eastern Cordillera. Comparison of basin subsidence with thermochronometric evidence of synchronous exhumation and mountain building suggests an incomplete understanding of the evolution of this archetypal retroarc foreland basin system. Results also highlight significant along-strike differences in foreland basin evolution: foredeep deposits are thinner, and the timing of high sediment accumulation rate is systematically later from north to south. Results considered in the context of magmatism, igneous geochemistry, and surface uplift records, tentatively support models of orogenic cyclicity. However, high-flux magmatic events in southern Peru are out of phase compared to those documented in northwest Argentina. Along-strike variability, controlled by structural Paleozoic–Mesozoic tectonic fabric preceding development of the Cenozoic Andean plateau, may control the rate of simple shear

underthrusting of continental lithospheric material and ultimately modulate the timing of orogenic cycles.

## ACKNOWLEDGEMENTS

We gratefully acknowledge assistance in southern Peru from Erick Gil and the Gil family. This work benefitted from fruitful discussions with Nadine McQuarrie, Nick Perez, Brian Horton, Margarete Jadamec, Tyson Smith, Nick Bartschi, and Noah Karsky. We thank Yongjun Gao and Minako Righter laboratory assistance. We thank Mauricio Parra, Emilio A. Rojas Vera, and an anonymous referee for detailed reviews which greatly improved the quality and clarity of this manuscript. We also thank Editor Taylor Schildgen and Associate Editor Marcelo Farias for the handling of this manuscript. All the data used can be found in the Supplemental Materials and listed in the references; new U-Pb geochronology data are also archived at geochron.org. The mixing model can be downloaded directly at <https://www.kurtsundell.com/downloads/> or <https://github.com/kurtsundell/DZmix>. Fieldwork and analytical costs were supported by grants from the National Science Foundation (EAR- 1550097), the National Geographic Society Committee for Research and Exploration, Geological Society of America Grants-in-Aid, International Association of Sedimentologists, Sigma Xi, and scholarships from the Joe and Lucy Steward Memorial Endowment, the Sam Penn Memorial Endowment, Houston Alumni Association, British Petroleum, and Marathon Oil Corporation.

## REFERENCES

- Allen, P. A., & Allen, J. R. (2013). *Basin analysis: Principles and application to petroleum play assessment*: John Wiley & Sons.
- Allmendinger, R. (2005). Stereonet. *Program for stereographic projection*.
- Allmendinger, R. W., Jordan, T. E., Kay, S. M., & Isacks, B. L. (1997). The evolution of the Altiplano-Puna plateau of the Central Andes. *Annual review of earth and planetary sciences*, 25(1), 139-174.
- Allmendinger, R. W., Ramos, V. A., Jordan, T. E., Palma, M., & Isacks, B. L. (1983). Paleogeography and Andean structural geometry, northwest Argentina. *Tectonics*, 2(1), 1-16.
- Antoine, P. O., Abello, M. A., Adnet, S., Sierra, A. J. A., Baby, P., Billet, G., & Corfu, F. (2016). A 60-million-year Cenozoic history of western Amazonian ecosystems in Contamana, eastern Peru. *Gondwana Research*, 31, 30-59.
- Arriagada, C., Roperch, P., Mpodozis, C., Dupont-Nivet, G., Cobbold, P. R., Chauvin, A., & Cortés, J. (2003). Paleogene clockwise tectonic rotations in the forearc of central Andes, Antofagasta region, northern Chile. *Journal of Geophysical Research: Solid Earth*, 108(B1).
- Baby, P., Rochat, P., Mascle, G., & Héral, G. (1997). Neogene shortening contribution to crustal thickening in the back arc of the Central Andes. *Geology*, 25(10), 883-886.
- Bahlburg, H., Vervoort, J. D., Du Frane, S. A., Bock, B., Augustsson, C., & Reimann, C. (2009). Timing of crust formation and recycling in accretionary orogens: Insights learned from the western margin of South America. *Earth-Science Reviews*, 97(1), 215-241.
- Bahlburg, H., Vervoort, J. D., DuFrane, S. A., Carlotto, V., Reimann, C., & Cárdenas, J. (2011). The U-Pb and Hf isotope evidence of detrital zircons of the Ordovician Ollantaytambo Formation, southern Peru, and the Ordovician provenance and paleogeography of southern Peru and northern Bolivia. *Journal of South American Earth Sciences*, 32(3), 196-209.
- Barnes, J., & Ehlers, T. (2009). End member models for Andean Plateau uplift. *Earth-Science Reviews*, 97(1), 105-132.
- Beck, S. L., & Zandt, G. (2002). The nature of orogenic crust in the central Andes. *Journal of Geophysical Research: Solid Earth*, 107(B10).
- Beck, S. L., Zandt, G., Myers, S. C., Wallace, T. C., Silver, P. G., & Drake, L. (1996). Crustal-thickness variations in the central Andes. *Geology*, 24(5), 407-410.
- Berry, E. W. (1917). The Age of the Bolivian Andes. *Proceedings of the National Academy of Sciences*, 3(4), 283-285.
- Bridge, J. S., & Best, J. L. (1988). Flow, sediment transport and bedform dynamics over the transition from dunes to upper-stage plane beds: implications for the formation of planar laminae. *Sedimentology*, 35(5), 753-763.
- Campbell, C. V. (1967). Lamina, laminaset, bed and bedset. *Sedimentology*, 8(1), 7-26.
- Carlotto, V. (1998). *Evolution andine et raccourcissement au niveau de Cusco (13°-16° S), Pérou: Enregistrement sédimentaire, chronologie, contrôles paléogéographiques, évolution cinématique*. Université Joseph-Fourier-Grenoble I,
- Carlotto, V. (2013). Paleogeographic and tectonic controls on the evolution of Cenozoic basins in the Altiplano and Western Cordillera of southern Peru. *Tectonophysics*, 589, 195-219.
- Carlotto, V., Cardénas, J., & Carlier, G. (2011). Geología del Cuadrángulo de Cusco 28-s-1: 50 000. INGEMMET. *Boletín, Serie A: Carta Geológica Nacional*, 138, 255.
- Carlotto, V., Carlier, G., Jaillard, E., Cardenas, J., Cerpa, L., Flores, T., & Latorre, O. (2005).

- Las cuencas terciarias sinorogénicas en el Altiplano y en la Cordillera Occidental. *Boletin de la Sociedad geologica del Perù*, 6(spécial), 103 à126.
- Carrapa, B., Bywater-Reyes, S., DeCelles, P. G., Mortimer, E., & Gehrels, G. E. (2012). Late Eocene–Pliocene basin evolution in the Eastern Cordillera of northwestern Argentina (25–26 S): regional implications for Andean orogenic wedge development. *Basin Research*, 24(3), 249-268.
- Carrapa, B., & DeCelles, P. G. (2015). Regional exhumation and kinematic history of the central Andes in response to cyclical orogenic processes. *Geological Society of America Memoirs*, 212, 201-213.
- Cawood, P. A., Hawkesworth, C., & Dhuime, B. (2012). Detrital zircon record and tectonic setting. *Geology*, 40(10), 875-878.
- Chapman, J. B., Ducea, M. N., DeCelles, P. G., & Profeta, L. (2015). Tracking changes in crustal thickness during orogenic evolution with Sr/Y: An example from the North American Cordillera. *Geology*, 43(10), 919-922.
- Chavez, R., Gil, W., Mamani, S., Sotomayor, M., Cardenas, J., & Carlotto, V. (1994). *Sedimentología y estratigrafía de la formación Punacancha (Eoceno?) en la región de Cusco*. In: VIII Congreso Peruano de Geología.
- Che, X., & Li, G. (2013). Binary sources of loess on the Chinese Loess Plateau revealed by U-Pb ages of zircon. *Quaternary Research*, 80(3), 545-551.
- Chew, D. M., Magna, T., Kirkland, C. L., Mišković, A., Cardona, A., Spikings, R., & Schaltegger, U. (2008). Detrital zircon fingerprint of the Proto-Andes: Evidence for a Neoproterozoic active margin? *Precambrian research*, 167(1), 186-200.
- Chew, D. M., Schaltegger, U., Košler, J., Whitehouse, M. J., Gutjahr, M., Spikings, R. A., & Miškovic, A. (2007). U-Pb geochronologic evidence for the evolution of the Gondwanan margin of the north-central Andes. *Geological Society of America Bulletin*, 119(5-6), 697-711.
- Currie, C. A., Ducea, M. N., DeCelles, P. G., & Beaumont, C. (2015). Geodynamic models of Cordilleran orogens: Gravitational instability of magmatic arc roots. *Geological Society of America Memoirs*, 212, 1-22.
- Dalrymple, R. W., & James, N. P. (2010). *Facies models 4*.
- Davis, D., Suppe, J., & Dahlen, F. (1983). Mechanics of fold-and-thrust belts and accretionary wedges. *Journal of Geophysical Research: Solid Earth*, 88(B2), 1153-1172.
- DeCelles, P., & DeCelles, P. (2001). Rates of shortening, propagation, underthrusting, and flexural wave migration in continental orogenic systems. *Geology*, 29(2), 135-138.
- Decelles, P. G. (2012). Foreland Basin Systems Revisited. In *Tectonics of Sedimentary Basins: Recent Advances*: John Wiley and Sons.
- DeCelles, P. G., Carrapa, B., Horton, B., & Gehrels, G. E. (2011). Cenozoic foreland basin system in the central Andes of northwestern Argentina: Implications for Andean geodynamics and modes of deformation. *Tectonics*, 30(6).
- DeCelles, P. G., Ducea, M. N., Kapp, P., & Zandt, G. (2009). Cyclicity in Cordilleran orogenic systems. *Nature Geoscience*, 2(4), 251-257.
- DeCelles, P. G., Zandt, G., Beck, S. L., Currie, C. A., Ducea, M. N., Kapp, P., ... & Schoenbohm, L. M. (2015). Cyclical orogenic processes in the Cenozoic central Andes. *Geological Society of America Memoirs*, 212, MWR212-22.
- DeCelles, P. G., & Giles, K. A. (1996). Foreland basin systems. *Basin research*, 8(2), 105-123.
- DeCelles, P. G., & Graham, S. (2015). Cyclical processes in the North American Cordilleran orogenic system. *Geology*, 43(6), 499-502.
- DeCelles, P. G., & Horton, B. K. (2003). Early to middle Tertiary foreland basin development and the history of Andean crustal shortening in Bolivia. *Geological*

*Society of America Bulletin*, 115(1), 58-77.

- DeCelles, P. G., Langford, R. P., & Schwartz, R. K. (1983). Two new methods of paleocurrent determination from trough cross-stratification. *Journal of Sedimentary Research*, 53(2).
- Decou, A., Von Eynatten, H., Dunkl, I., Frei, D., & Wörner, G. (2013). Late Eocene to Early Miocene Andean uplift inferred from detrital zircon fission track and U-Pb dating of Cenozoic forearc sediments (15–18 S). *Journal of South American Earth Sciences*, 45, 6-23.
- Deeken, A., Sobel, E. R., Coutand, I., Haschke, M., Riller, U., & Strecker, M. R. (2006). Development of the southern Eastern Cordillera, NW Argentina, constrained by apatite fission track thermochronology: From early Cretaceous extension to middle Miocene shortening. *Tectonics*, 25(6).
- Demouy, S., Paquette, J.-L., de Saint Blanquat, M., Benoit, M., Belousova, E. A., O'Reilly, S. Y., Sempere, T. (2012). Spatial and temporal evolution of Liassic to Paleocene arc activity in southern Peru unraveled by zircon U-Pb and Hf in-situ data on plutonic rocks. *Lithos*, 155, 183-200.
- Dickinson, W. R., & Gehrels, G. E. (2009). Use of U-Pb ages of detrital zircons to infer maximum depositional ages of strata: a test against a Colorado Plateau Mesozoic database. *Earth and Planetary Science Letters*, 288(1), 115-125.
- Dickinson, W. R., & Suczek, C. A. (1979). Plate tectonics and sandstone compositions. *Aapg Bulletin*, 63(12), 2164-2182.
- Diepenbroek, M., Bartholomä, A., & Ibbeken, H. (1992). How round is round? A new approach to the topic ‘roundness’ by Fourier grain shape analysis. *Sedimentology*, 39(3), 411-422.
- Ducea, M. N., & Barton, M. D. (2007). Igniting flare-up events in Cordilleran arcs. *Geology*, 35(11), 1047-1050.
- Ducea, M. N., Paterson, S. R., & DeCelles, P. G. (2015). High-volume magmatic events in subduction systems. *Elements*, 11(2), 99-104.
- Ege, H., Sobel, E. R., Scheuber, E., & Jacobshagen, V. (2007). Exhumation history of the southern Altiplano plateau (southern Bolivia) constrained by apatite fission track thermochronology. *Tectonics*, 26(1).
- Ehlers, T. A., & Poulsen, C. J. (2009). Influence of Andean uplift on climate and paleoaltimetry estimates. *Earth and Planetary Science Letters*, 281(3), 238-248.
- Forbes, D. (1861). On the geology of Bolivia and southern Peru. *Quarterly Journal of the Geological Society*, 17(1-2), 7-62.
- Garzione, C. N., Hoke, G. D., Libarkin, J. C., Withers, S., MacFadden, B., Eiler, J., . . . Mulch, A. (2008). Rise of the Andes. *science*, 320(5881), 1304-1307.
- Garzione, C. N., Molnar, P., Libarkin, J. C., & MacFadden, B. J. (2006). Rapid late Miocene rise of the Bolivian Altiplano: Evidence for removal of mantle lithosphere. *Earth and Planetary Science Letters*, 241(3), 543-556.
- Garzione, C. N., McQuarrie, N., Perez, N. D., Ehlers, T. A., Beck, S. L., Kar, N., . . . Lease, R. O. (2017). Tectonic evolution of the Central Andean plateau and implications for the growth of plateaus. *Annual Review of Earth and Planetary Sciences*, 45, 529-559.
- Gazzi, P. (1966). The upper Cretaceous Flysch sandstones (Modena Apennine); comparison with the Monghidoro Flysch. *Mineral. Petrogr. Acta*, 12, 69-97.
- Gehrels, G. (2014). Detrital zircon U-Pb geochronology applied to tectonics. *Annual Review of Earth and Planetary Sciences*, 42, 127-149.
- Gillis, R. J., Horton, B. K., & Grove, M. (2006). Thermochronology, geochronology, and upper crustal structure of the Cordillera Real: Implications for Cenozoic exhumation of the central Andean plateau. *Tectonics*, 25(6).

- Göğüş, O. H., & Pysklywec, R. N. (2008). Mantle lithosphere delamination driving plateau uplift and synconvergent extension in eastern Anatolia. *Geology*, 36(9), 723-726.
- Gotberg, N., McQuarrie, N., & Caillaux, V. C. (2010). Comparison of crustal thickening budget and shortening estimates in southern Peru (12–14 S): Implications for mass balance and rotations in the “Bolivian orocline”. *Bulletin*, 122(5-6), 727-742.
- Hampton, B. A., & Horton, B. K. (2007). Sheetflow fluvial processes in a rapidly subsiding basin, Altiplano plateau, Bolivia. *Sedimentology*, 54(5), 1121-1148.
- Haschke, M., Günther, A., Melnick, D., Echtler, H., Reutter, K.-J., Scheuber, E., & Oncken, O. (2006). Central and southern Andean tectonic evolution inferred from arc magmatism. In *The Andes* (pp. 337-353): Springer.
- Haschke, M., Siebel, W., Günther, A., & Scheuber, E. (2002). Repeated crustal thickening and recycling during the Andean orogeny in north Chile (21–26 S). *Journal of Geophysical Research: Solid Earth*, 107(B1).
- Hazewinkel, M. (2001). Student t-test. *Encyclopedia of Mathematics*, Springer, Berlin, Germany, ISBN, 978-971.
- Horton, B., Hampton, B., LaReau, B., & Baldellon, E. (2002). Tertiary provenance history of the northern and central Altiplano (central Andes, Bolivia): A detrital record of plateau-margin tectonics. *Journal of Sedimentary Research*, 72(5), 711-726.
- Horton, B., Hampton, B., & Waanders, G. (2001). Paleogene synorogenic sedimentation in the Altiplano plateau and implications for initial mountain building in the central Andes. *Geological Society of America Bulletin*, 113(11), 1387-1400.
- Horton, B. K., & DeCelles, P. G. (1997). The modern foreland basin system adjacent to the Central Andes. *Geology*, 25(10), 895-898.
- Horton, B. K., Perez, N. D., Fitch, J. D., & Saylor, J. E. (2015). Punctuated shortening and subsidence in the Altiplano Plateau of southern Peru: Implications for early Andean mountain building. *Lithosphere*, 7(2), 117-137.
- Isacks, B. L. (1988). Uplift of the central Andean plateau and bending of the Bolivian orocline. *Journal of Geophysical Research: Solid Earth*, 93(B4), 3211-3231.
- Jordán, T. E., Isacks, B. L., Allmendinger, R. W., Brewer, J. A., Ramos, V. A., & Ando, C. J. (1983). Andean tectonics related to geometry of subducted Nazca plate. *Geological Society of America Bulletin*, 94(3), 341-361.
- Kar, N., Garzione, C. N., Jaramillo, C., Shanahan, T., Carlotto, V., Pullen, A., . . . Eiler, J. (2016). Rapid regional surface uplift of the northern Altiplano plateau revealed by multiproxy paleoclimate reconstruction. *Earth and Planetary Science Letters*, 447, 33-47.
- Kay, R. W., & Kay, S. M. (1993). Delamination and delamination magmatism. *Tectonophysics*, 219(1), 177-189.
- Kay, S. M., Coira, B., & Viramonte, J. (1994). Young mafic back arc volcanic rocks as indicators of continental lithospheric delamination beneath the Argentine Puna plateau, central Andes. *Journal of Geophysical Research: Solid Earth*, 99(B12), 24323-24339.
- Košler, J., Longerich, H. P., & Tubrett, M. N. (2002). Effect of oxygen on laser-induced elemental fractionation in LA-ICP-MS analysis. *Analytical and bioanalytical chemistry*, 374(2), 251-254.
- Krumbein, W. C. (1941). Measurement and geological significance of shape and roundness of sedimentary particles. *Journal of Sedimentary Research*, 11(2).
- Krystopowicz, N. J., & Currie, C. A. (2013). Crustal eclogitization and lithosphere delamination in orogens. *Earth and Planetary Science Letters*, 361, 195-207.
- Lamb, S. (2011). Did shortening in thick crust cause rapid Late Cenozoic uplift in the northern Bolivian Andes? *Journal of the Geological Society*, 168(5), 1079-1092.

- Mamani, M., Tassara, A., & Wörner, G. (2008). Composition and structural control of crustal domains in the central Andes. *Geochemistry, Geophysics, Geosystems*, 9(3).
- Mamani, M., Wörner, G., & Sempere, T. (2010). Geochemical variations in igneous rocks of the Central Andean orocline (13 S to 18 S): Tracing crustal thickening and magma generation through time and space. *Geological Society of America Bulletin*, 122(1-2), 162-182.
- McGroder, M. F., Lease, R. O., & Pearson, D. M. (2015). Along-strike variation in structural styles and hydrocarbon occurrences, Subandean fold-and-thrust belt and inner foreland, Colombia to Argentina. *Geological Society of America Memoirs*, 212, 79-113.
- Miall, A. (2010). *The geology of stratigraphic sequences*: Springer Science & Business Media.
- Miall, A. D. (1977). Lithofacies types and vertical profile models in braided river deposits: a summary.
- Molnar, P., & Lyon-Caen, H. (1988). Some simple physical aspects of the support, structure, and evolution of mountain belts. *Geological Society of America Special Papers*, 218, 179-208.
- Mourier, T., Bengtson, P., Bonhomme, M., Buge, E., Cappetta, H., Crochet, J., . . . Laubacher, G. (1988). The Upper Cretaceous-Lower Tertiary marine to continental transition in the Bagua basin, northern Perú. *Newsletters on Stratigraphy*, 19, 143-177.
- Muhlbauer, J. G., Fedo, C. M., & Farmer, G. L. (2017). Influence of textural parameters on detrital-zircon age spectra with application to provenance and paleogeography during the Ediacaran–Terreneuvian of southwestern Laurentia. *Geological Society of America Bulletin*, B31611. 31611.
- Newell, N. D. (1946). Geological investigations around Lake Titicaca. *American Journal of Science*, 244(5), 357-366.
- Newell, N. D. (1949). Geology of the lake Titicaca region, Peru and Bolivia. *Geological Society of America Memoirs*, 36, 1-124.
- Nilsen, T. H., & Sylvester, A. G. (1999). Strike-slip basins: Part 1. *The Leading Edge*, 18(10), 1146-1152.
- Oncken, O., Hindle, D., Kley, J., Elger, K., Victor, P., & Schemmann, K. (2006). Deformation of the central Andean upper plate system—Facts, fiction, and constraints for plateau models. In *The Andes* (pp. 3-27): Springer.
- Paces, J. B., & Miller, J. D. (1993). Precise U-Pb ages of Duluth complex and related mafic intrusions, northeastern Minnesota: Geochronological insights to physical, petrogenetic, paleomagnetic, and tectonomagmatic processes associated with the 1.1 Ga midcontinent rift system. *Journal of Geophysical Research: Solid Earth*, 98(B8), 13997-14013.
- Pardo-Casas, F., & Molnar, P. (1987). Relative motion of the Nazca (Farallon) and South American plates since Late Cretaceous time. *Tectonics*, 6(3), 233-248.
- Perelló, J., Carlotto, V., Zárate, A., Ramos, P., Posso, H., Neyra, C., . . . Muhr, R. (2003). Porphyry-style alteration and mineralization of the middle Eocene to early Oligocene Andahuaylas-Yauri Belt, Cuzco region, Peru. *Economic Geology*, 98(8), 1575-1605.
- Perez, N. D., & Horton, B. K. (2014). Oligocene-Miocene deformational and depositional history of the Andean hinterland basin in the northern Altiplano plateau, southern Peru. *Tectonics*, 33(9), 1819-1847.
- Perez, N. D., Horton, B. K., & Carlotto, V. (2016a). Structural inheritance and selective reactivation in the central Andes: Cenozoic deformation guided by pre-Andean structures in southern Peru. *Tectonophysics*, 671, 264-280.

- Perez, N. D., Horton, B. K., McQuarrie, N., Stuebner, K., & Ehlers, T. A. (2016b). Andean shortening, inversion and exhumation associated with thin-and thick-skinned deformation in southern Peru. *Geological Magazine*, 153(5-6), 1013-1041.
- Peterman, Z. E., & Sims, P. (1988). The Goodman Swell: A lithospheric flexure caused by crustal loading along the Midcontinent Rift System. *Tectonics*, 7(5), 1077-1090.
- Pilger, R. H. (1984). Cenozoic plate kinematics, subduction and magmatism: South American Andes. *Journal of the Geological Society*, 141(5), 793-802.
- Profeta, L., Ducea, M. N., Chapman, J. B., Paterson, S. R., Gonzales, S. M. H., Kirsch, M., . . . DeCelles, P. G. (2015). Quantifying crustal thickness over time in magmatic arcs. *Scientific reports*, 5.
- Rak, A. J., McQuarrie, N., & Ehlers, T. A. (2017). Kinematics, Exhumation, and Sedimentation of the North Central Andes (Bolivia): An Integrated Thermochronometer and Thermokinematic Modeling Approach. *Tectonics*, 36(11), 2524-2554.
- Ramos, V. A. (2009). Anatomy and global context of the Andes: Main geologic features and the Andean orogenic cycle. *Geological Society of America Memoirs*, 204, 31-65.
- Ramos, V. A., & Folguera, A. (2009). Andean flat-slab subduction through time. Geological Society, London, Special Publications, 327(1), 31-54.
- Ramos, V. A., Litvak, V. D., Folguera, A., & Spagnuolo, M. (2014). An Andean tectonic cycle: From crustal thickening to extension in a thin crust (34–37 SL). *Geoscience Frontiers*, 5(3), 351-367.
- Reimann, C., Bahlburg, H., Kooijman, E., Berndt, J., Gerdes, A., Carlotto, V., & López, S. (2010). Geodynamic evolution of the early Paleozoic Western Gondwana margin 14–17 S reflected by the detritus of the Devonian and Ordovician basins of southern Peru and northern Bolivia. *Gondwana Research*, 18(2), 370-384.
- Rousse, S., Gilder, S., Fornari, M., & Sempere, T. (2005). Insight into the Neogene tectonic history of the northern Bolivian Orocline from new paleomagnetic and geochronologic data. *Tectonics*, 24(6).
- Saylor, J. E., & Horton, B. K. (2014). Nonuniform surface uplift of the Andean plateau revealed by deuterium isotopes in Miocene volcanic glass from southern Peru. *Earth and Planetary Science Letters*, 387, 120-131.
- Saylor, J. E., Knowles, J. N., Horton, B. K., Nie, J., & Mora, A. (2013). Mixing of source populations recorded in detrital zircon U-Pb age spectra of modern river sands. *The Journal of Geology*, 121(1), 17-33.
- Saylor, J. E., Jordan, J. C., Sundell, K. E., Wang, X., Wang, S., & Deng, T. (2017). Topographic growth of the Jishi Shan and its impact on basin and hydrology evolution, NE Tibetan Plateau. *Basin Research*.
- Saylor, J. E., & Sundell, K. E. (2016). Quantifying comparison of large detrital geochronology data sets. *Geosphere*, GES01237. 01231.
- Schoenbohm, L. M., & Strecker, M. R. (2009). Normal faulting along the southern margin of the Puna Plateau, northwest Argentina. *Tectonics*, 28(5).
- Shaulis, B., Lapen, T. J., & Toms, A. (2010). Signal linearity of an extended range pulse counting detector: Applications to accurate and precise U-Pb dating of zircon by laser ablation quadrupole ICP-MS. *Geochemistry, Geophysics, Geosystems*, 11(11).
- Sláma, J., Košler, J., Condon, D. J., Crowley, J. L., Gerdes, A., Hanchar, J. M., . . . Schaltegger, U. (2008). Plešovice zircon—a new natural reference material for U–Pb and Hf isotopic microanalysis. *Chemical Geology*, 249(1-2), 1-35.
- Soler, P., & Bonhomme, M. G. (1990). Relation of magmatic activity to plate dynamics in central Peru from Late Cretaceous to present. *Geological Society of America Special Papers*, 241, 173-192.

Accepted Article

- Stacey, J. T., & Kramers, I. (1975). Approximation of terrestrial lead isotope evolution by a two-stage model. *Earth and planetary science letters*, 26(2), 207-221.
- Stephens, M. A. (1970). Use of the Kolmogorov-Smirnov, Cramér-Von Mises and related statistics without extensive tables. *Journal of the Royal Statistical Society. Series B (Methodological)*, 115-122.
- Sundell, K. E., & Saylor, J. E. (2017). Unmixing detrital geochronology age distributions. *Geochemistry, Geophysics, Geosystems.*, 18, doi:10.1002/2016GC006774.
- Takashimizu, Y., & Iiyoshi, M. (2016). New parameter of roundness R: circularity corrected by aspect ratio. *Progress in Earth and Planetary Science*, 3(1), 2.
- Vermeesch, P. (2013). Multi-sample comparison of detrital age distributions. *Chemical Geology*, 341, 140-146.
- Xie, X., & Heller, P. L. (2009). Plate tectonics and basin subsidence history. *Geological Society of America Bulletin*, 121(1-2), 55-64.

Table 1

## *Lithofacies Classifications*

Lithofacies code	Observation	Interpretation
c	Thinly laminated or structureless claystone	Suspension settling, swam deposits
Fm(c)	Structureless mudstone (c indicates carbonaceous)	Overbank deposits and suspension settling, often redistributed by post-depositional bioturbation
Fl	Laminated mudstone	Overbank, waning flood, or abandoned channel deposits
Sm	Structureless sandstone	Rapid sand deposition without stable bedform development, or post depositional redistribution via bioturbation
Sr	Assymetric ripple cross-stratified sandstone	Migrating 2-D or 3-D ripple bedforms in lower flow regime unidirectional flow in shallow channels
St	Trough cross-stratified sandstone	Migration of sinuous-crested and lingoid dunes in subaqueous unidirectional flow
Sh	Horizontally laminated sandstone	Supercritical upper flow regime plane bed flow of high velocity $\geq 100$ cm/s or in very shallow water
Gmm	Matrix-supported structureless poorly sorted disorganized conglomerate	Plastic or cohesive (high strength) debris flow, buoyancy modified sand sheet and hyperconcentrated flow
Gcm	Clast-supported structureless poorly sorted disorganized conglomerate	Pseudoplastic debris flow, clast rich, pressure or buoyancy modified sheet flood deposition
Gcmi	Clast-supported conglomerate, structureless and imbricated	Traction transport of migrating subaqueous barforms in unsteady flow
Gchi	Clast-supported conglomerate, crudely horizontally bedded, imbricated (i)	Deposition by shallow traction currents, longitudinal barforms and gravel sheets or lag deposits

Table 2  
*Sandstone petrography modal point-counting parameters*

Symbol	Description
Qm	Monocrystalline quartz
Qp	Polycrystalline quartz
Qpt	Polycrystalline foliated quartz
P	Plagioclase feldspar
K	Alkali feldspar (perthitic, orthoclase and sanidine)
Km	Alkali feldspar (microcline)
Lsc	Lithic siliciclastic claystone
Lss	Lithic siliciclastic siltstone
Lcl	Lithic carbonate limestone
Lch	Lithic chert
Lv	Lithic volcanics
Lpb	Lithic plutonic gabbroic
Lpg	Lithic plutonic granitic
Lms	Lithic metamorphic slate
Lmp	Lithic metamorphic
Lmg	Lithic metamorphic gneiss
Apx	Accessory mineral (pyroxene group)
Aam	Accessory mineral (amphibole group)
Amu	Accessory mineral (muscovite)
Azn	Accessory mineral (zircon)
Amg	Accessory mineral (magnetite)

*Q Total quartz (Qm + Qp + Qms + Lch)*

*F Total feldspar (K + P)*

*Lv Total volcanic lithic fragments (Lv<sub>f</sub> + Lv<sub>i</sub> + Lv<sub>m</sub> + Lv<sub>l</sub>)*

*Lm Total metamorphic lithic fragments (Lmg + Lmf + Lmn)*

*Ls Total sedimentary lithic fragments (Lsc + Lss + Lsm)*

*L Total lithic fragments (Lv + Lm + Ls)*

*Lt Total lithic fragments with chert (Lv + Lm + Ls + Lch)*

Table 3  
*Sandstone petrography results*

Sample Name	Stratigraphic level (m)	Q	F	L	Qm	F	L	Qm	P	K	Qp	Lv	Ls
20150518-01	125	66	21	13	61	24	14	72	28	0	48	44	7
20150519-03	260	25	29	46	20	31	49	39	60	1	12	57	32
20150519-05	430	39	30	31	34	32	34	51	49	0	21	48	31
20150519-06	530	34	37	29	29	40	31	42	58	0	18	58	23
20150520-01	610	16	40	43	13	42	45	24	72	4	8	80	12
20150520-02	720	27	21	53	13	24	62	35	57	7	23	69	8
20150520-03	800	34	28	39	26	31	43	45	54	1	21	57	21
20150520-04	920	12	28	60	6	30	64	17	76	7	10	75	16
20150520-05	1060	30	42	28	23	46	31	33	64	3	24	64	12
20150521-01	1190	14	45	41	10	47	43	17	80	2	10	78	12
20150521-02	1250	19	39	42	17	40	43	29	67	4	6	83	11
20150521-03	1310	19	41	39	15	44	41	26	73	1	12	65	23
20150523-01	1470	30	28	42	29	28	43	51	45	4	3	74	22
20150523-02	1530	33	31	36	30	32	38	48	52	0	12	72	16
20150523-03	1640	15	47	37	13	49	38	21	75	3	7	74	19
20150523-04	1750	11	47	41	5	51	44	9	88	3	14	72	14
20150525-02	1830	40	28	32	36	30	34	55	44	1	15	71	15
20150525-01	1980	28	42	30	22	46	33	32	68	0	22	67	11
20150525-03	2040	26	43	32	13	50	37	20	79	0	32	58	10
20150525-05	2180	9	53	38	0	58	42	0	83	17	19	69	12
20150526-01	2320	24	56	20	18	60	22	23	76	1	27	64	9
20150526-02	2460	23	45	32	15	50	35	23	77	0	24	69	7
20150526-03	2580	19	43	38	16	45	39	26	74	0	9	84	7
20150527-01	2770	20	50	30	17	52	31	24	75	1	12	85	3
20150527-03	2840	4	68	28	1	70	29	1	91	8	10	84	6

20150527-04	2920	29	51	20	24	55	21	31	69	0	26	45	30
20150527-05	3090	8	45	47	2	48	50	4	93	3	11	80	10
20150528-01	3220	9	51	40	1	56	43	2	97	1	16	78	6
20140611-01	3600	12	51	36	8	54	38	14	86	0	10	73	17
20140611-02	4170	19	51	30	13	55	32	19	81	0	20	62	17
20140611-03	4800	9	54	37	5	57	38	8	92	0	11	78	11
20140605-01	4900	69	25	6	66	27	7	71	29	0	63	9	29
20140603-01	5330	36	41	23	32	44	25	42	57	1	23	46	31
20140604-01	5450	34	35	32	30	37	33	45	54	0	15	65	20
20140607-01	5800	27	28	46	21	30	49	41	59	0	15	52	33
20140608-01	5890	20	29	51	15	31	54	33	67	0	9	45	46
20140608-03	6100	27	31	43	21	33	46	39	60	0	14	55	31

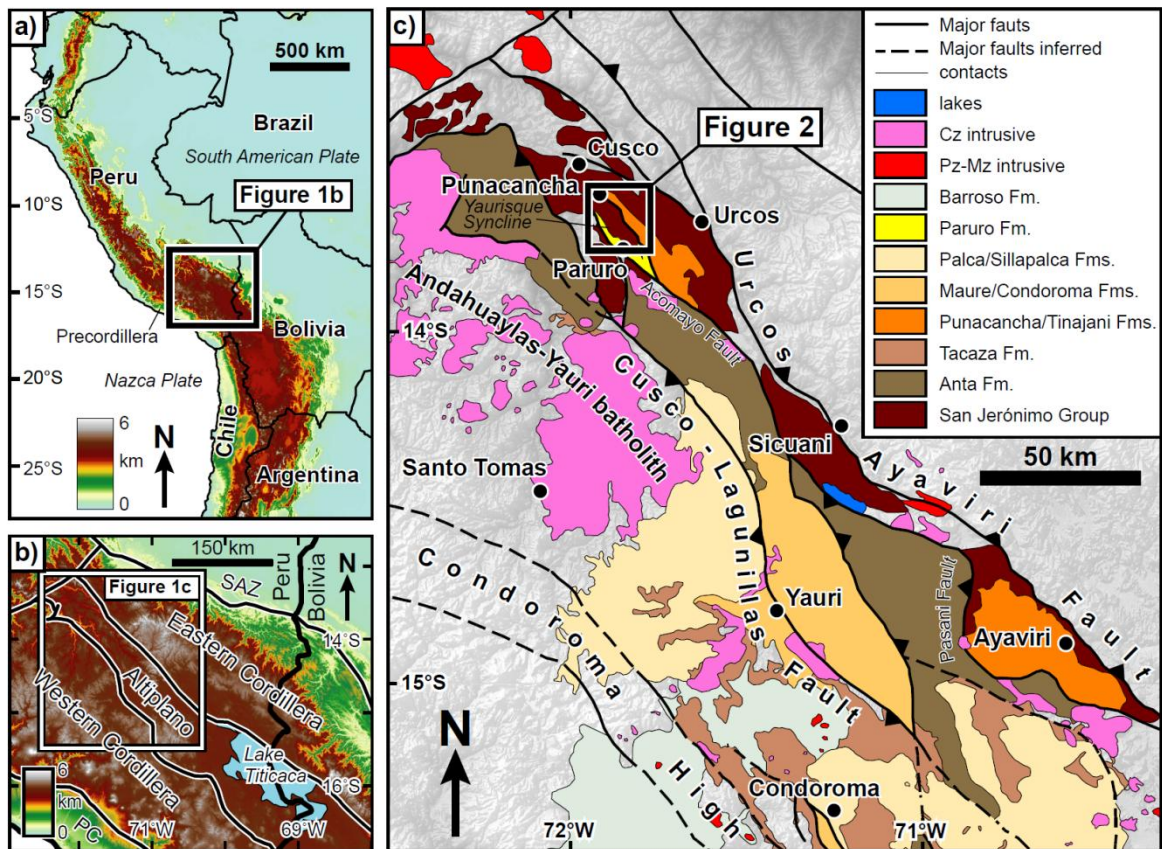
Accepted

Table 4

*Detrital zircon U-Pb sample data*

Data Source	Sample name	Physiographic region	Latitude	Longitude	Formation (Fm.) or group (Gp.) name	Geologic age	n	Rock type
<i>this study</i>	20140608-03	Altiplano	-13.76799	-71.82979	Top Paruro Fm.	L. Miocene	299	Sandstone
<i>this study</i>	20140528-01		-13.75312	-71.83511			258	Sandstone
<i>this study</i>	20140605-01	Altiplano	-13.75913	-71.82329	Base Paruro Fm.	Miocene	141	Sandstone
<i>this study</i>	20140605-02		-13.75969	-71.82277			19	Sandstone
<i>this study</i>	20140611-03	Altiplano	-13.62829	-71.88537	Top Punacancha Fm.	L. Oligocene	234	Sandstone
<i>this study</i>	20140611-01	Altiplano	-13.61641	-71.87318	Base Punacancha Fm.	Oligocene	324	Sandstone
<i>this study</i>	20150525-02	Altiplano	-13.61761	-71.84363	Soncco Fm.	L. Eocene	356	Sandstone
<i>this study</i>	20150520-01	Altiplano	-13.69650	-71.85138	Kayra Fm.	Eocene	306	Sandstone
<i>this study</i>	20150519-03	Altiplano	-13.69364	-71.84798	Quilque Fm.	L. Paleocene	313	Sandstone
<i>this study</i>	20160813-08	Altiplano	-16.05183	-69.77223	Huancané Fm.	E. Cretaceous	316	Sandstone
Reimann et al. (2010)	La1	Altiplano	-15.29212	-70.33677	Lampa Fm.	Devonian	75	Sandstone
Reimann et al. (2010)	Cab6	Altiplano	-15.62735	-70.38471			107	Sandstone
	Cab18		-15.63089	-70.38242	Cabanillas Gp.	Devonian	88	Sandstone
Reimann et al. (2010)	Ja7	Altiplano	-15.31527	-70.24419	Calapuja Fm.	Ordovician	120	Sandstone
<i>this study</i>	20160814-	Western	-	-70.19324	Hualhuani Fm.	E. Cretaceous	209	Quartzite

	15	Cordillera	16.27508					
	20160815-06		-15.86207	-70.44615			121	Quartzite
<i>this study</i>	20160815-04	Western Cordillera	-15.85268	-70.30539	Labra Fm.	L. Jurassic	304	Quartzite
<i>this study</i>	20160815-05	Western Cordillera	-15.86480	-70.42625	Puente Fm.	L. Jurassic	303	Quartzite
Perez and Horton (2014)	NPPR12-25	Eastern Cordillera	-14.37551	-70.54854			92	Sandstone
	NPDZP003		-14.89772	-70.53311	Muni Fm.	E. Cretaceous	89	Sandstone
Perez and Horton (2014)	NPDZP006	Eastern Cordillera	-13.85975	-70.51526	Mitu Gp.	Permo-Triassic	96	Sandstone
Perez and Horton (2014)	NPDZP004	Eastern Cordillera	-14.35608	-70.55628	Ambo Fm.	E. Carboniferous	98	Sandstone
Perez and Horton (2014)	TC054	Eastern Cordillera	-14.84825	-70.56136	San Gaban Fm.	Ordovician	113	Sandstone
Bahlburg et al. (2011)	Oy13	Eastern Cordillera	-13.21600	-72.58700	Ollantaytambo Fm.	Ordovician	118	
Reimann et al. (2010)	San 12	Eastern Cordillera	-14.14366	-69.28065			118	Sandstone
	San 17		-14.25353	-69.40898	Sandia Fm.	Ordovician	111	Sandstone
Reimann et al. (2010)	Coro 18	Eastern Cordillera	-16.26904	-67.82120			124	Sandstone
	Am 20		-16.32674	-67.97069	Amutara Fm.	Ordovician	127	Sandstone



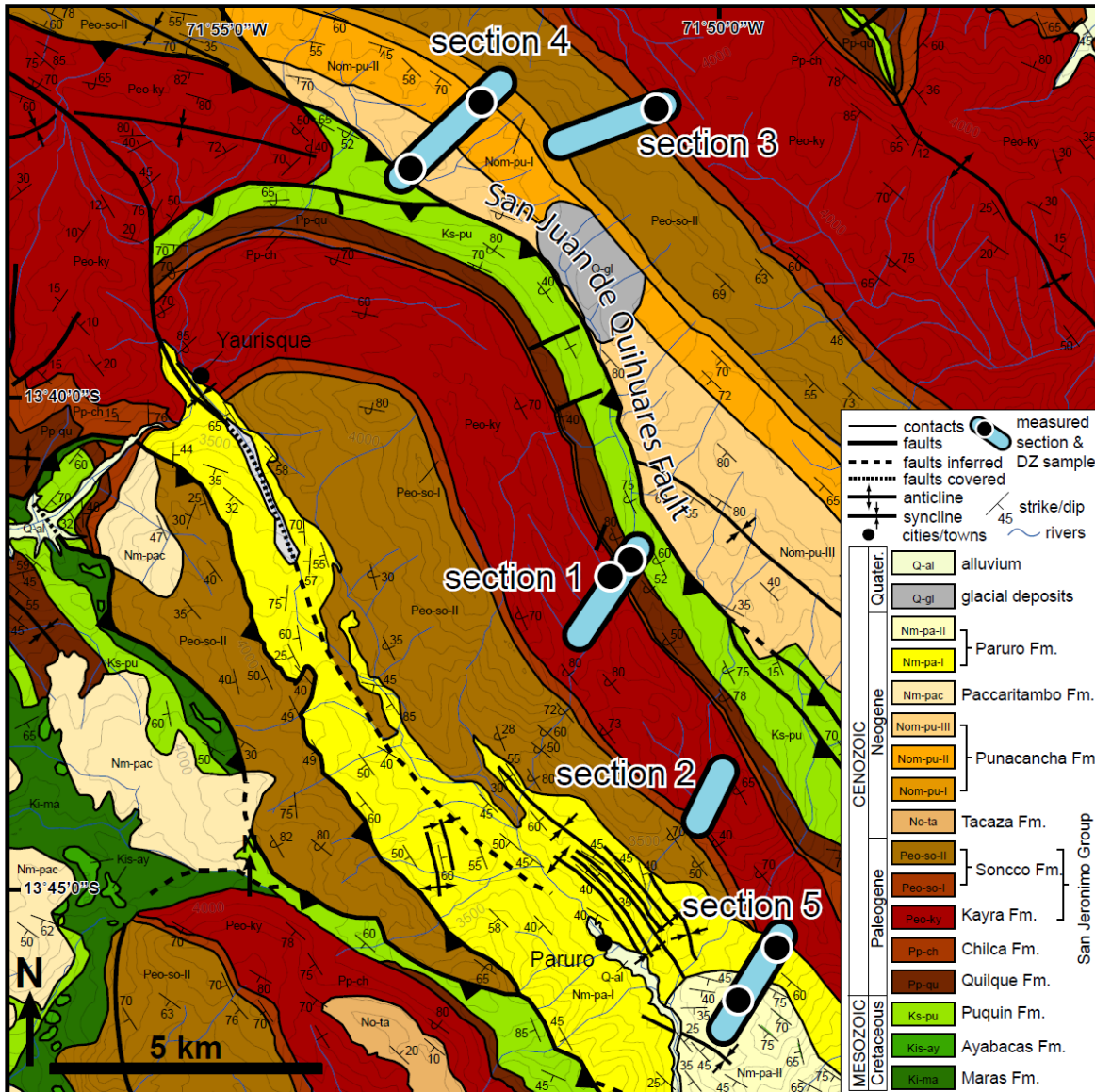


**Figure 2.** Geologic map of the study area modified from the Instituto Geológico Minero y Metalúrgico (INGEMMET) and Carlotto (2013) (see location in Figure 1). DZ = Detrital zircon.

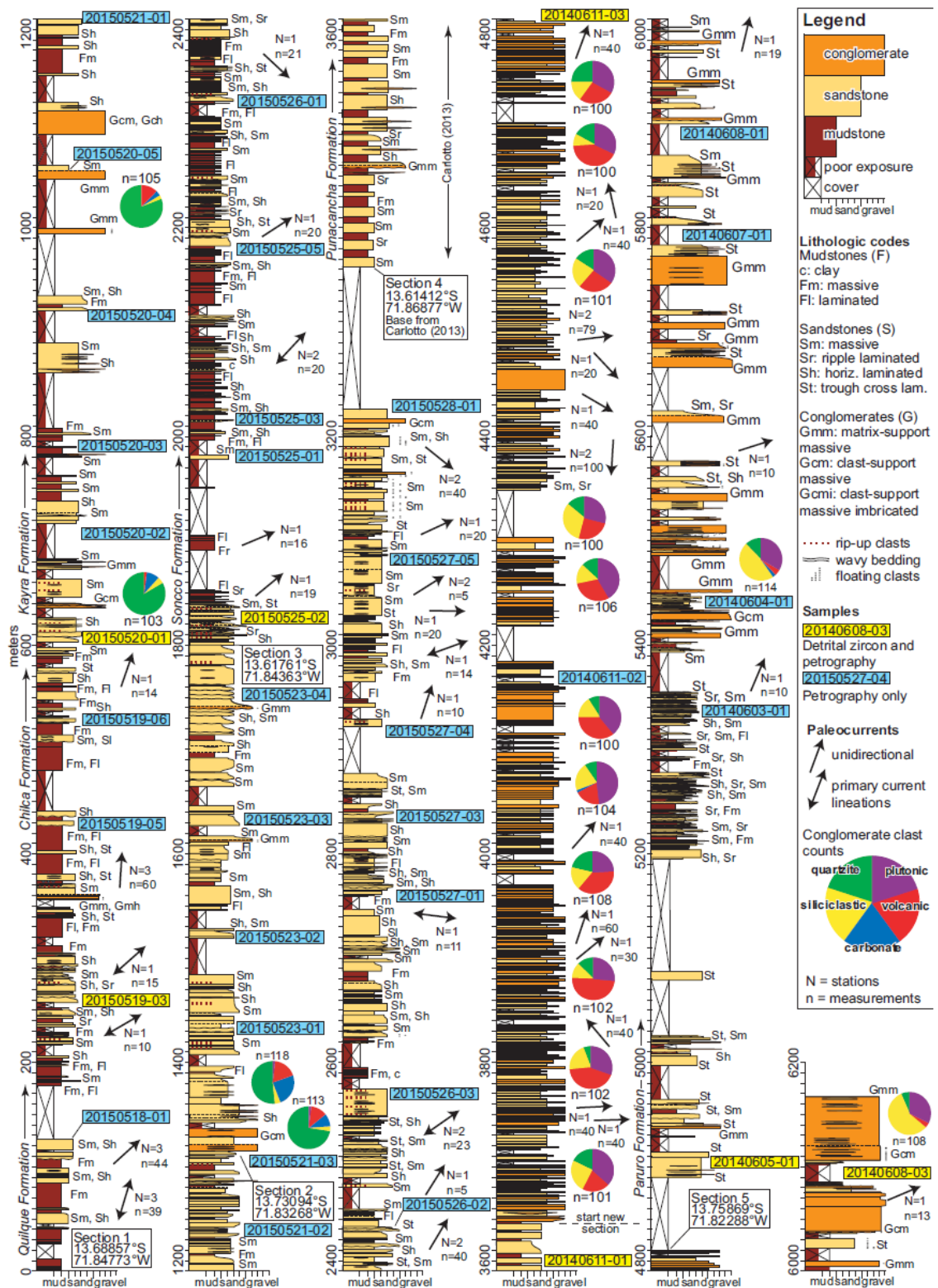


**Figure 3.** Composite Cenozoic stratigraphic section of the northernmost Altiplano showing lithofacies codes to the right corresponding to observations and interpretations of depositional

processes listed in Table 1 and described in Section 3.1.1. The base of each section is specified by the beginning of the formation name to the left of the section. Paleocurrent data are shown as black arrows (north is up, arrow points toward sediment transport direction; N = stations, n = individual measurements). Conglomerate clast count results are shown as pie diagrams.

Accepted Article

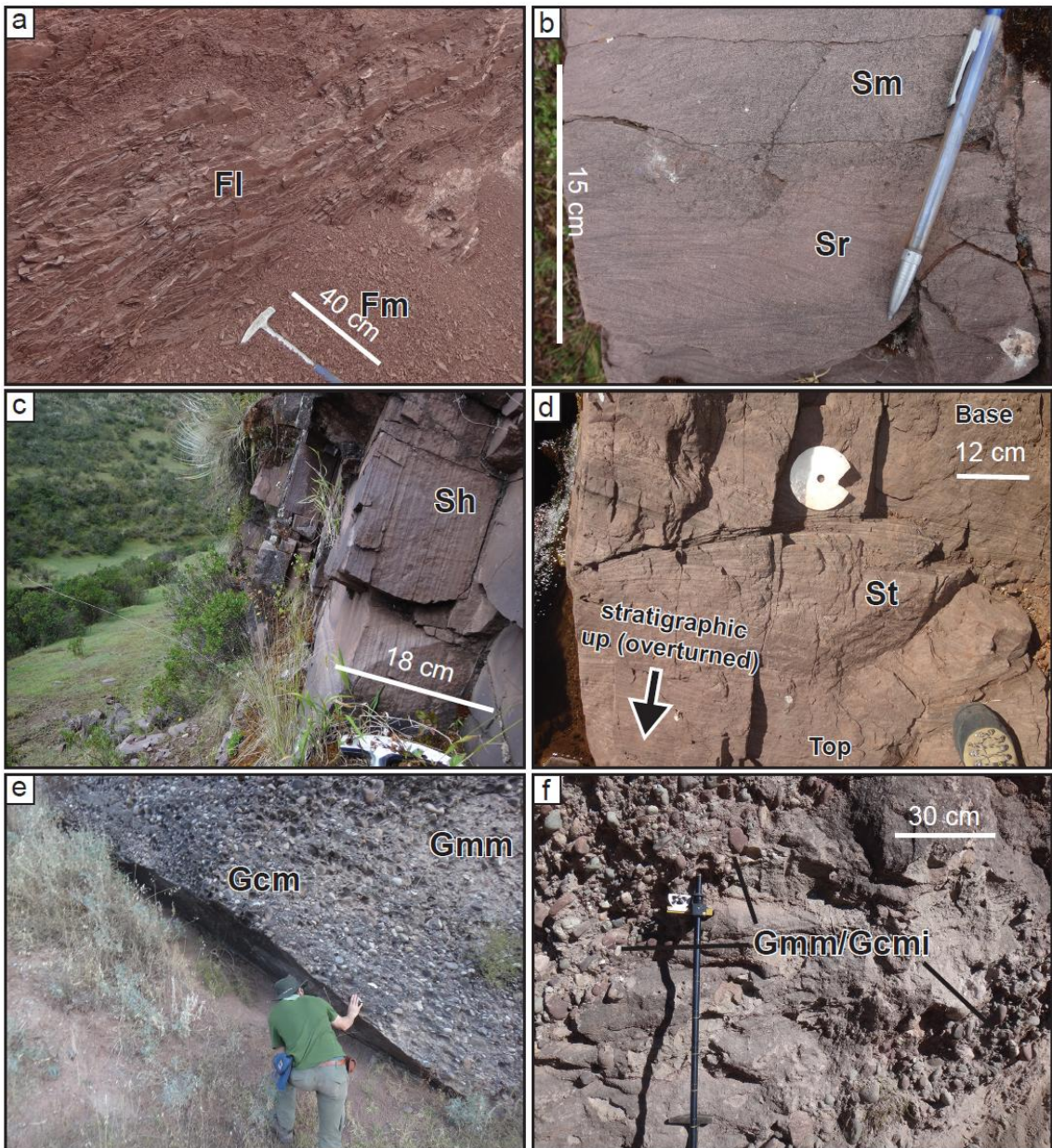


**Figure 4.** Photographs of key lithofacies listed in Table 1. (a) Fm/Fl: Alternating layers of massive and laminated siltstone. (b) Sm/Sr: Massive and ripple-cross-stratified sandstone. (c) Sh: Horizontally-laminated sandstone. (d) St: Trough-cross-stratified sandstone. (e) Gmm and Gcm: Matrix- and clast-supported conglomerate. (f) Gmm and Gcmi: Mixture of structureless and clast-supported imbricated conglomerates.

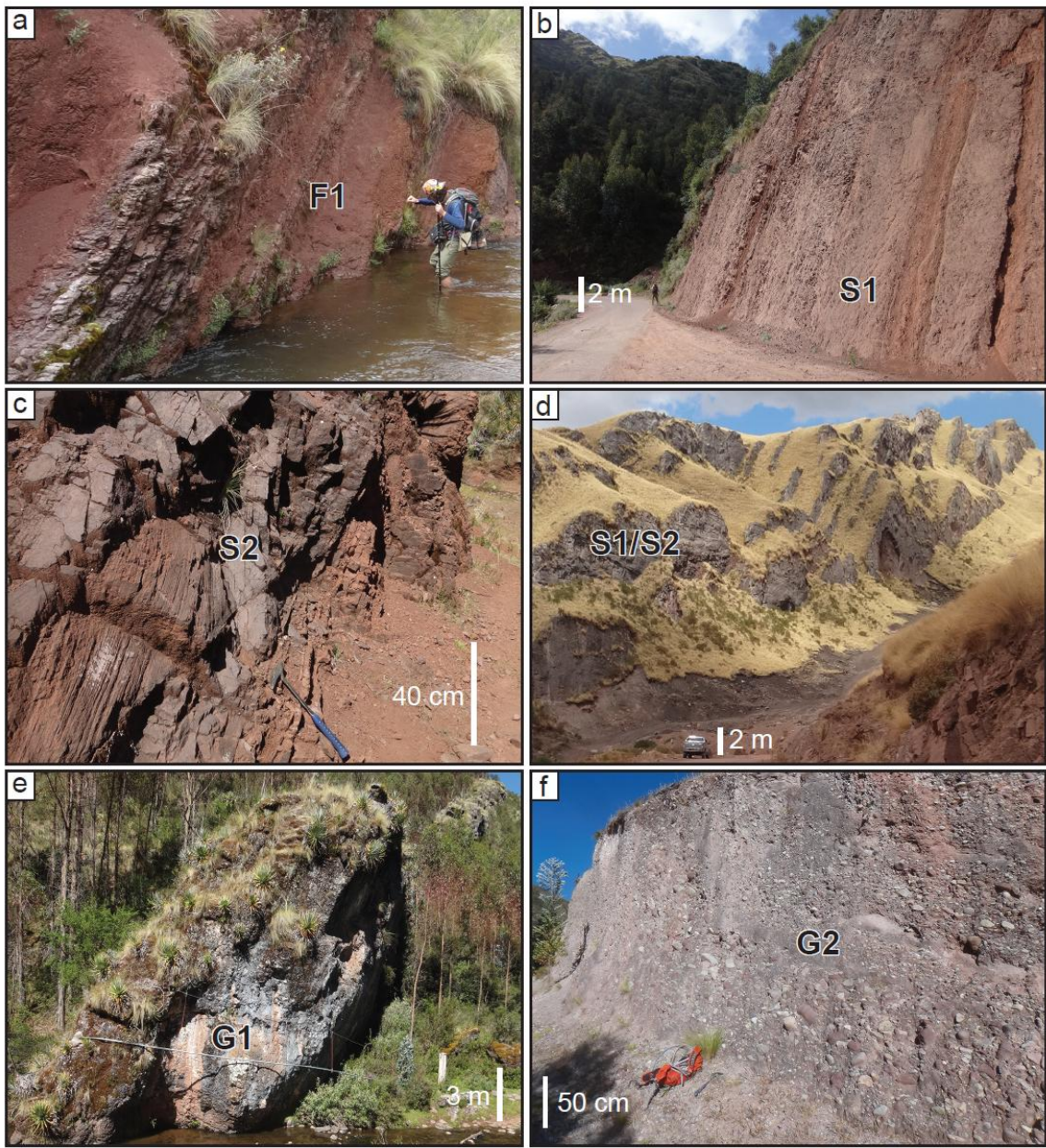


**Figure 5.** Photographs of key lithofacies associations. (a) Lithofacies association F1: thick packages of Fm and Fl mudstones with thinly interbedded very-fine–fine grained tabular Sm and Sh sandstones. (b) Lithofacies S1: thick, tabular sandstone sheets dominated by non-erosive Sm and Sh sandstones with limited St, with lesser interbedded mudstones; bedding bases typically show little basal scour. (c) Lithofacies association S2: Dominantly St, Sh, and Sm sandstones with limited Fm and Fl mudstones, typically with basal scour. (d) Laterally continuous sandstone units, characteristic of the Cusco, Peru area and other Altiplano basins

(e.g., Hampton & Horton, 2007). (e) Lithofacies association G1: dominantly Gcm and lesser Gmm conglomerate with a sharp, non-erosive base (also see Figure 4e). (f) Lithofacies association G2: mixture of Gmm, Gcm, Gcni, and Gchi.

Accepted Article

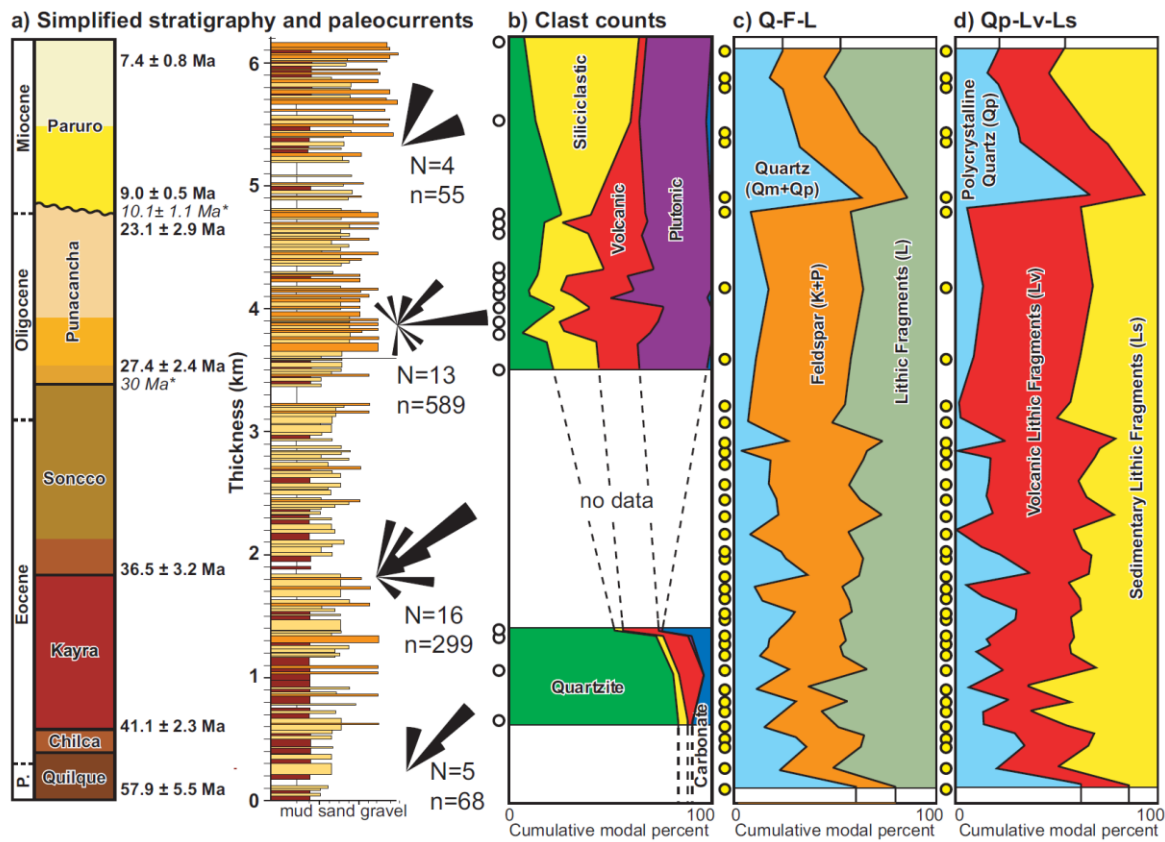


**Figure 6.** Summary of sedimentology and stratigraphy results. (a) Simplified composite stratigraphic section and combined paleocurrent rose diagrams for Quilque-Chilca, Kayra-Soncco, Punacancha, and Paruro formations ( $N$  = number of stations,  $n$  = number of individual measurements). Maximum depositional ages from detrital zircon U-Pb geochronology are in bold to the right of the stratigraphic section (\* indicates published ages, Carlotto, 2013). (b) Cumulative clast-count results showing up-section changes in conglomerate clast composition. White circles are sample locations plotted stratigraphically. (c) Sandstone petrography quartz-feldspar-lithic fragment (Q-F-L) results shown cumulatively. (d) Sandstone petrography polycrystalline quartz-volcanic lithics-sedimentary lithics (Qp-Lv-Ls) shown cumulatively. Yellow circles are sample locations plotted stratigraphically for parts c and d.

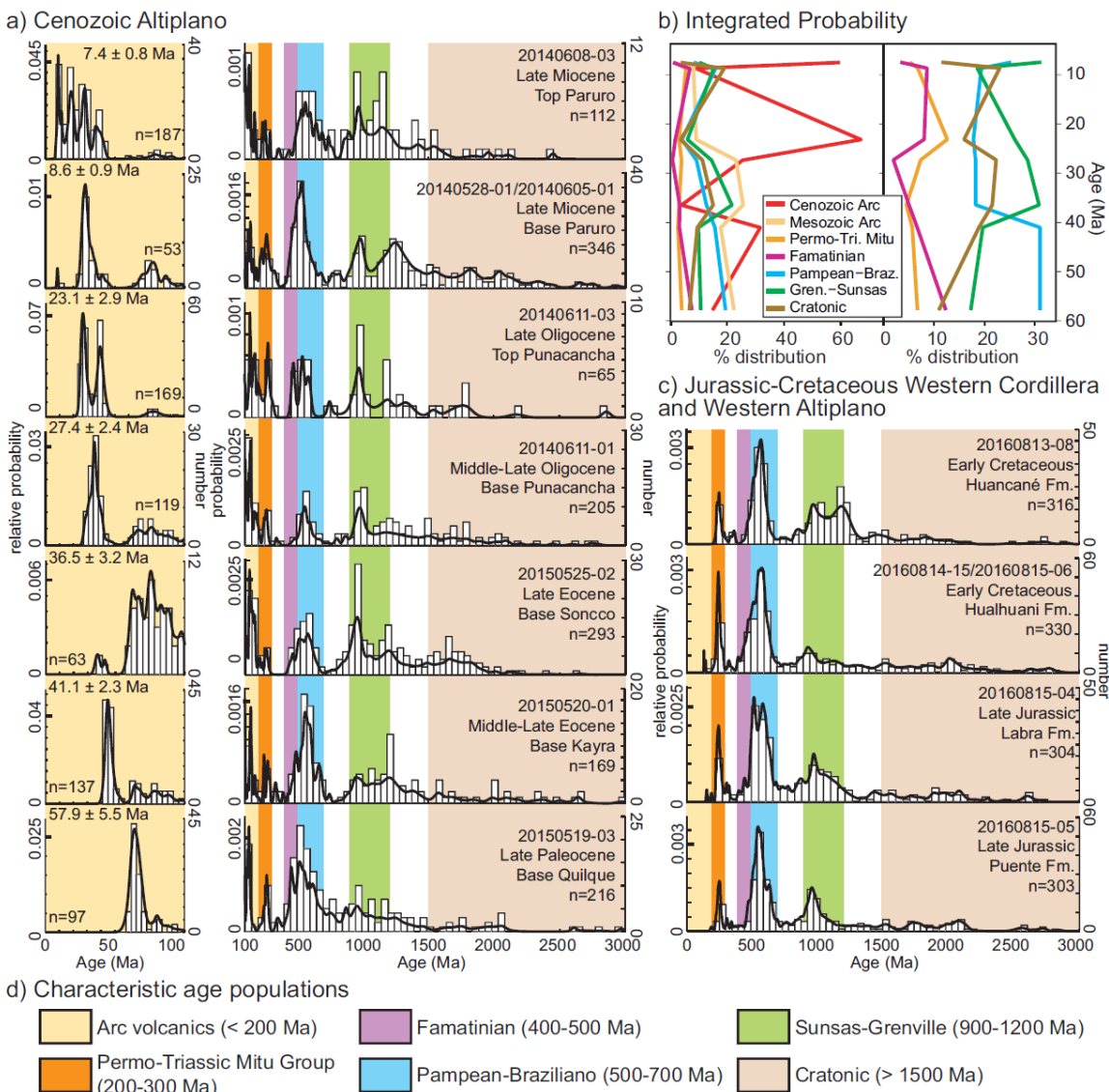


**Figure 7.** Detrital zircon U-Pb geochronology results shown as probability density plots (black lines) and histograms (white bars), and characteristic sediment source detrital zircon U-Pb age groups. (a) Detrital zircon U-Pb results for sandstone samples collected from Cenozoic Altiplano basin strata. Note the change in scale between ages 0–100 Ma and 100–3000 Ma; the former are typically an order of magnitude higher due to ongoing late Cretaceous–Cenozoic volcanism. Single-grain maximum depositional ages shown for each sample; n = number of ages. (b) Left: integrations of Cenozoic Altiplano detrital zircon probability density plots (Figure 7a) by characteristic age groups plotted against maximum

depositional age. Right: integrations with ages  $< 200$  Ma removed to enhance the older provenance signal. (c) Detrital zircon U-Pb results for quartzite samples collected from Jurassic–Cretaceous potential source samples from the Western Cordillera and western Altiplano. d) Characteristic sediment source groups (from Perez & Horton, 2014 and references therein).

Accepted Article

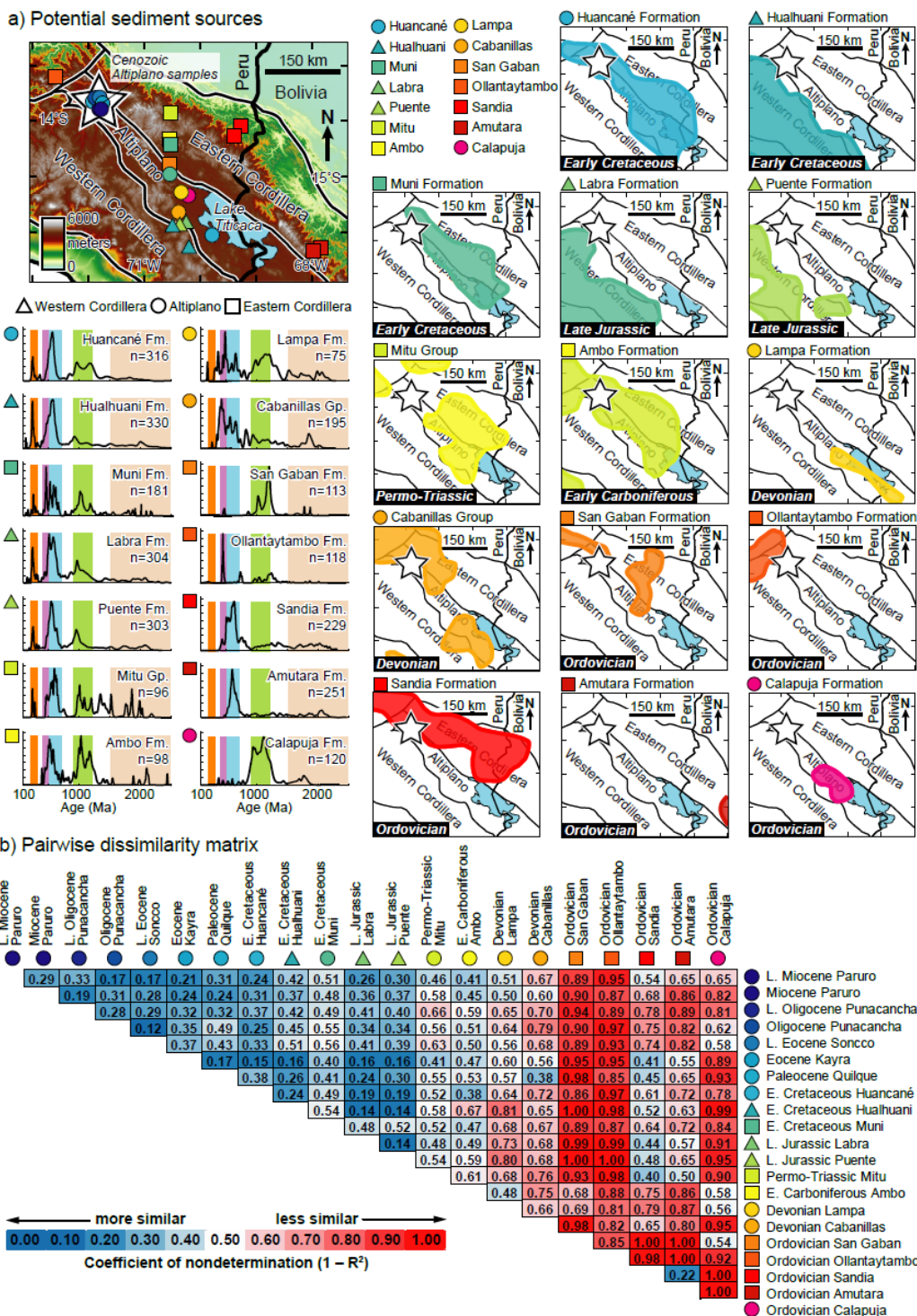
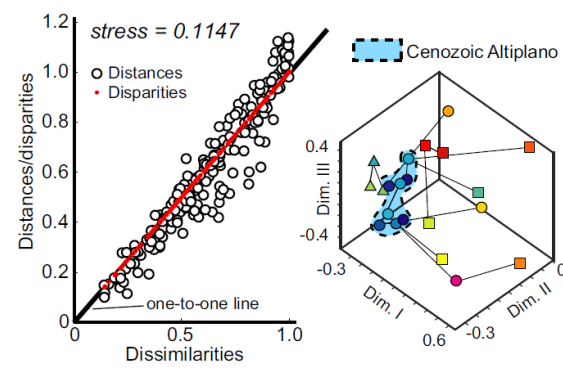


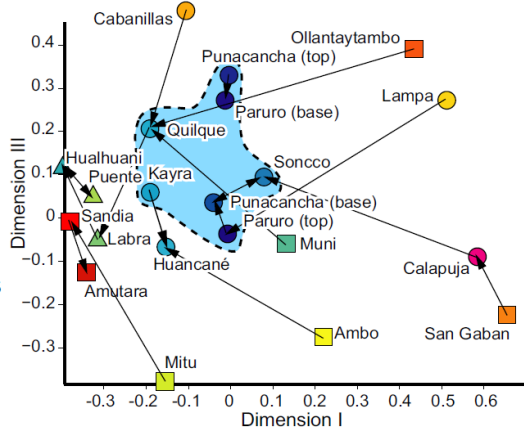
**Figure 8.** (a) Regional compilation of detrital zircon U-Pb data and locations of potential sediment source formations. Color bars indicate characteristic source groups as in Figure 7d. (b) Pairwise dissimilarity matrix calculated using 1 – Cross correlation coefficient (Saylor & Sundell, 2016).

### Multidimensional scaling (MDS)

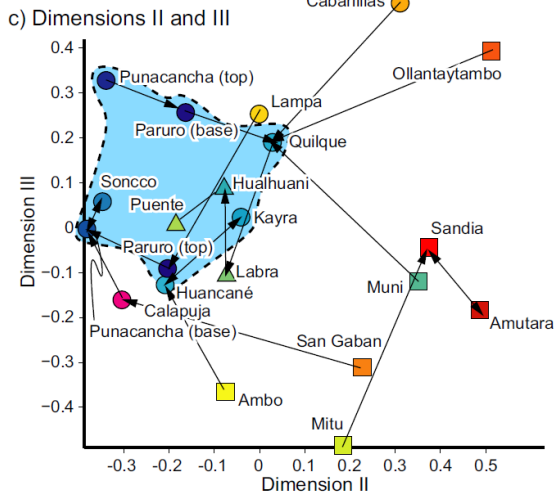
#### a) Shepard plot and 3D MDS



#### b) Dimensions I and III



#### c) Dimensions II and III



#### d) Dimensions I and II

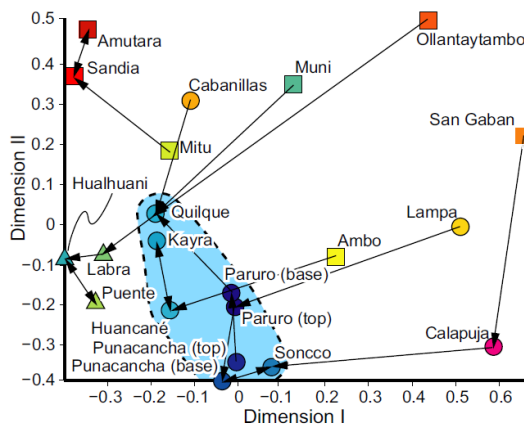


**Figure 9.** Three-dimensional (3D) multidimensional scaling (MDS) results using the pairwise dissimilarity matrix in Figure 8b. (a) Shepard plot and 3D MDS showing transformation from dissimilarity to distances and disparities. A low stress level of 0.1147 indicates a reasonable transformation. Light blue polygon corresponds to rough outlines of Cenozoic Altiplano samples in parts B–D. (b) Dimensions I and III from 3D MDS results. (c) Dimensions II and III from 3D MDS results. (d) Dimensions I and II from 3D MDS results. Black arrows indicate samples' nearest neighbor. Note the similarity in Cenozoic Altiplano samples to one another indicating minimal change in sediment source through time, as well as their similarity to Jurassic–Mesozoic formations indicating potentially large sediment contributions from these sources, and relatively limited sourcing from most of the Paleozoic formations. Also note the Calapuja Formation's nearest neighbor is the Soncco Formation, indicating it may have been significant sediment to the northern Altiplano at ~36 Ma.

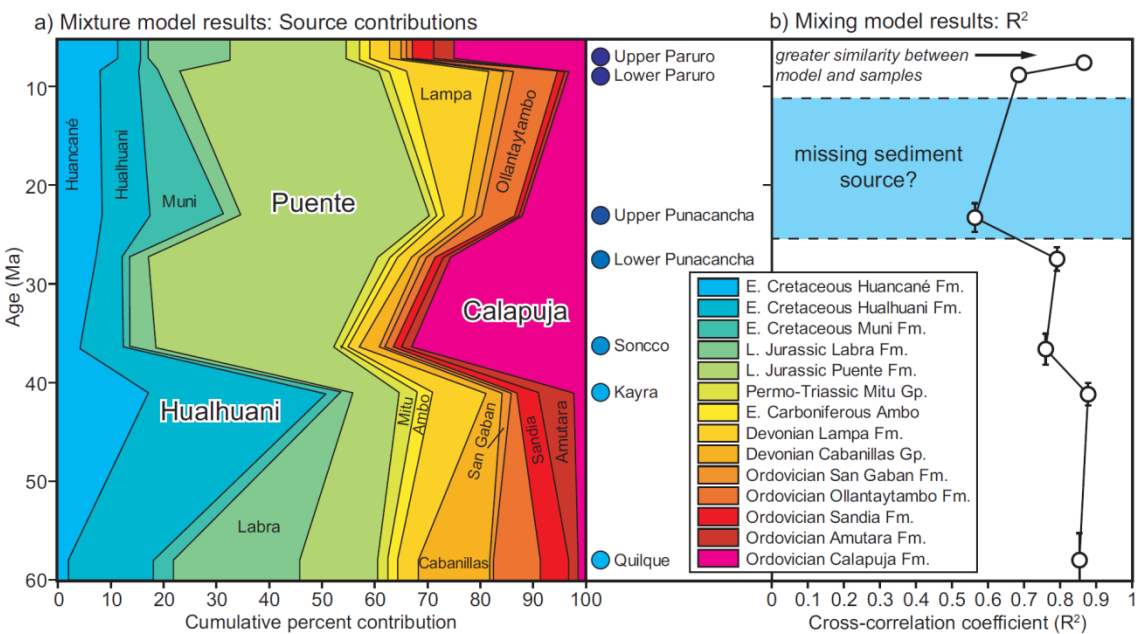


**Figure 10.** Detrital zircon U-Pb age distribution mixture modeling results using methods outlined in Sundell & Saylor (2017). (a) Up-section changes in source contribution shown cumulatively with younger formations on the left and older on the right. Note the predominance of sediment sourcing from the Hualhuani, Puente, and Calapuja formations. Also note that Jurassic and younger sources account for nearly 60% of sediment sourced in the Altiplano throughout the Cenozoic. (b) Maximum depositional age plotted against cross-correlation  $R^2$  for the top 100 of 100,000 model fits for each sample (0.1%). The model is able to reproduce Cenozoic Altiplano age distributions reasonably well (as indicated by a high  $R^2$  value), except for the upper Punacancha and lower Paruro formations. The former may be due to low sample size of ages  $> 200$  Ma ( $n = 56$ ); both model misfits may be due to a missing sediment source not included in the data compilation.

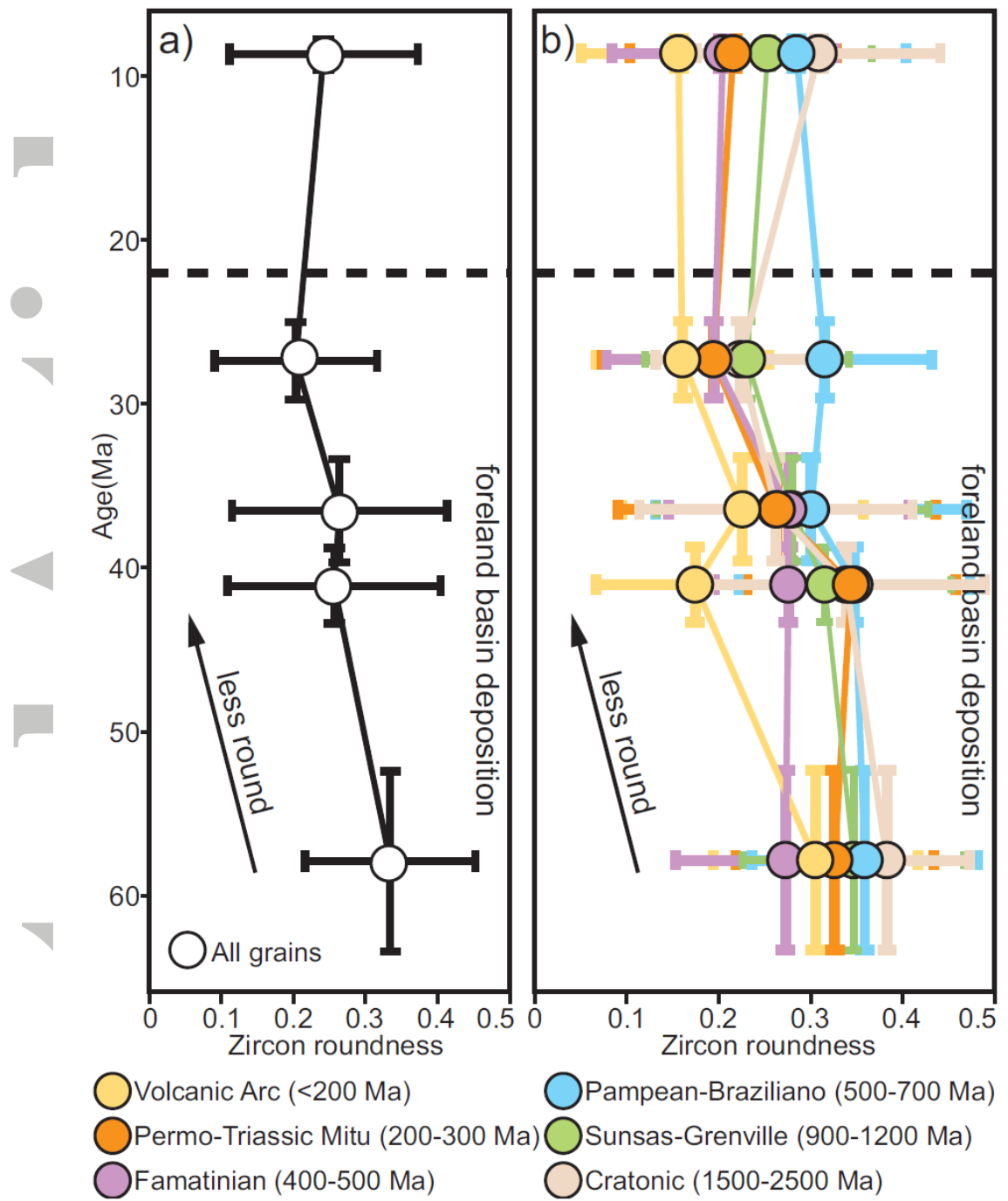


**Figure 11.** Zircon roundness results. (a) Maximum deposition age versus mean and  $1\sigma$  standard deviation zircon roundness. (b) Maximum depositional age versus mean roundness of grains divided into characteristic age groups. The Paleogene up-section decrease in roundness is consistent with a decrease in sediment transport distance as cratonward migration of the retroarc fold-and-thrust belt and magmatic arc brings sediment sources closer to the study location.

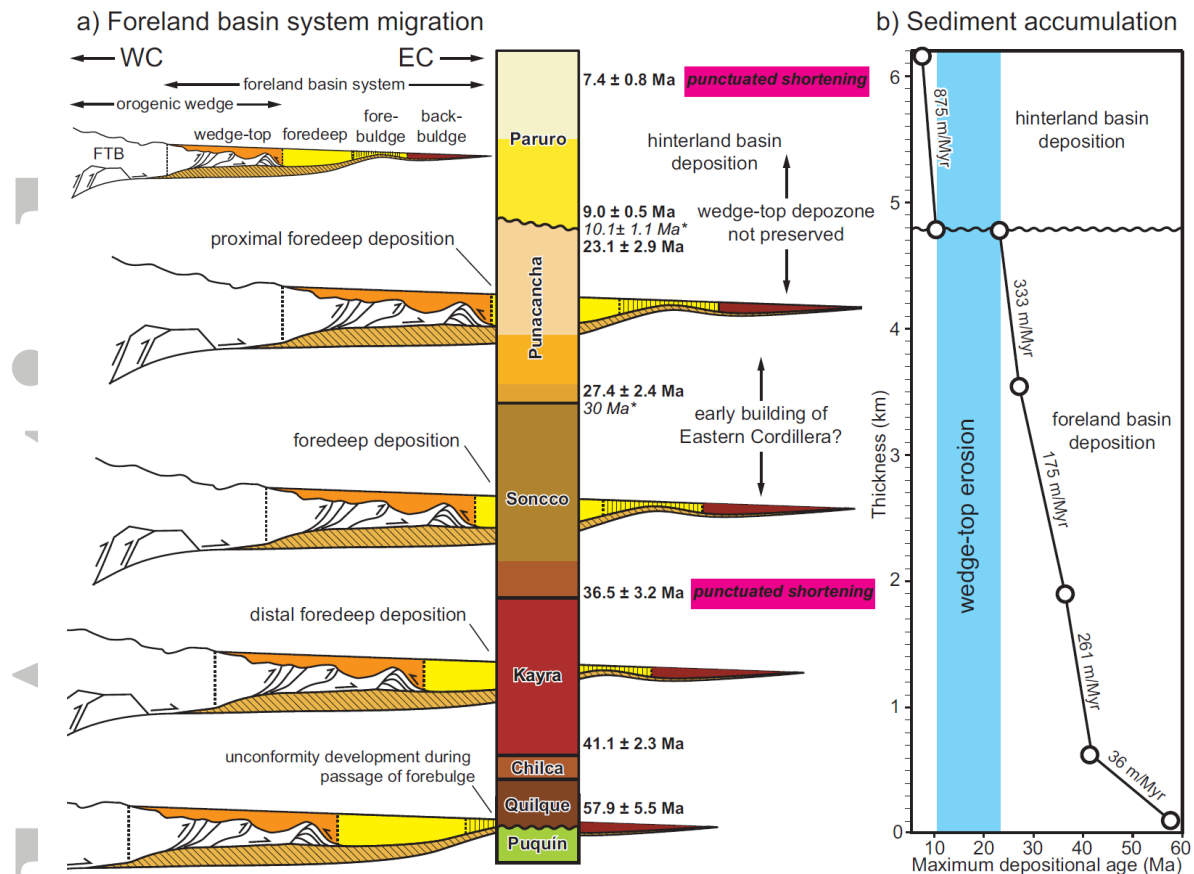


**Figure 12.** a) Foreland basin evolution in the context of a migrating foreland basin system (DeCelles & Giles, 1996). WC = Western Cordillera. EC = Eastern Cordillera. Timing of punctuated shortening (magenta boxes) inferred from mixture modeling (see Sections 4.2.3 and 4.3). b) Sediment accumulation rates calculated from measured sediment thicknesses and detrital zircon U-Pb maximum depositional ages (note that sediment compaction has not been taken into account).

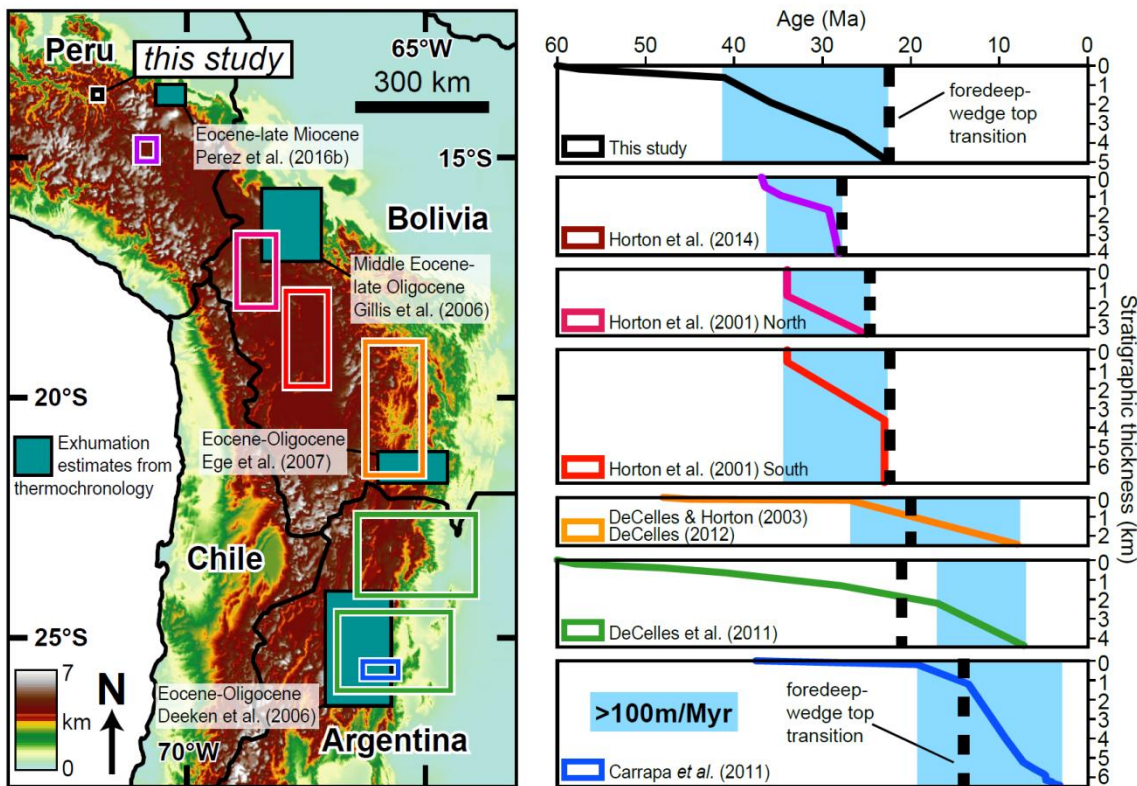


**Figure 13.** Sediment accumulation curves of foreland basin strata documented in the modern Altiplano and Eastern Cordillera for the Andean plateau. Note the systematically younger onset of rapid subsidence to the south and thicker foredeep deposits in the north.

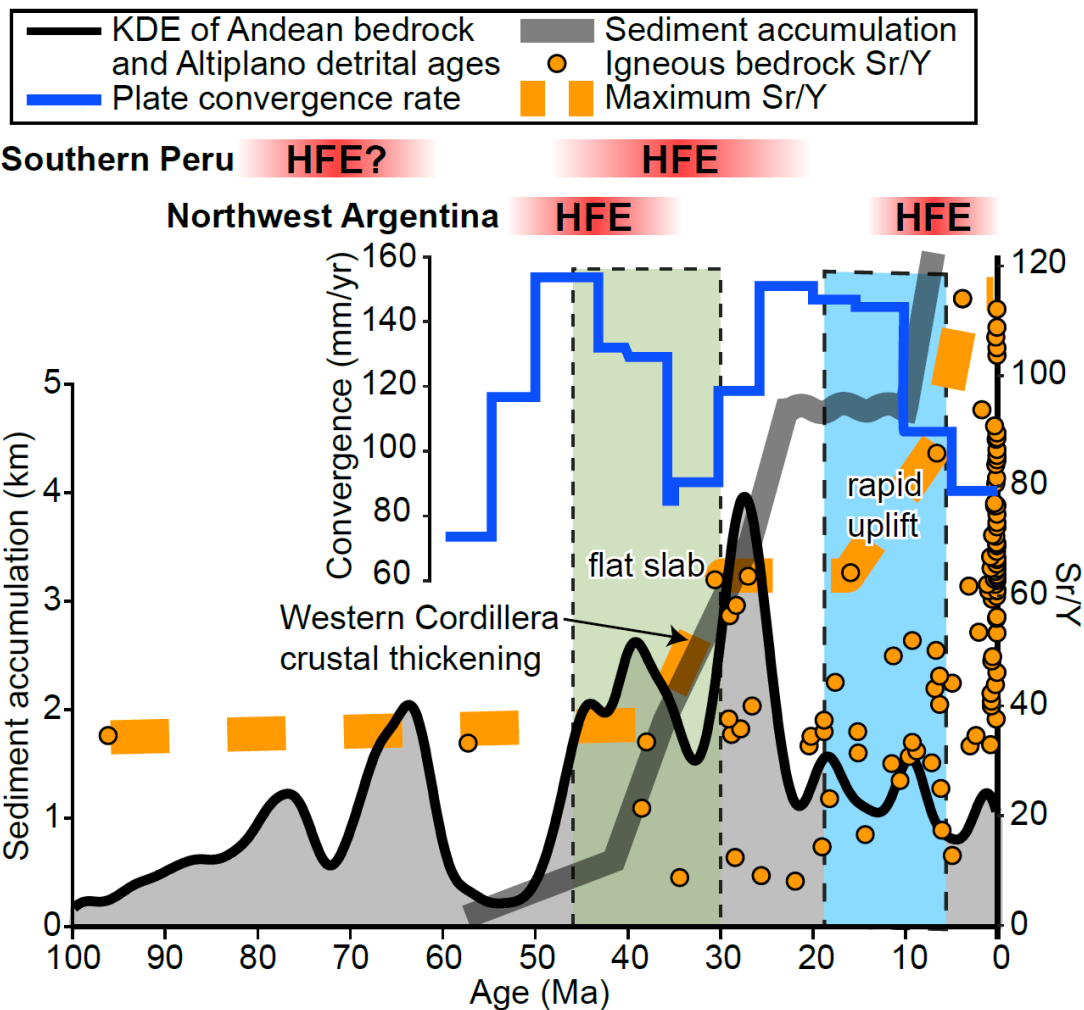


**Figure 14.** Compilation of data from southern Peru in the context of the orogenic cyclicity model (DeCelles et al., 2015). Kernel density estimate (KDE, black curve) of combined ages from Cenozoic Altiplano detrital zircon U-Pb samples and Andean igneous bedrock ages (from 13–18° S) compiled from the Central Andes Geochemical and Geochronology Database (<http://andes.gzg.geo.uni-goettingen.de/>) (constructed using a 3 Myr kernel). HFE = high-flux event. Plate convergence rates (in blue) from Pardo-Casas & Molnar (1987) do not correlate with apparent cyclicity. Sr/Y data (orange circles) were filtered to exclude samples containing  $\text{SiO}_2 > 65$  wt. % to avoid differentiation effects on trace elements. Yellow triangles are broadly coarsening upward packages in the Cenozoic Altiplano (Figure 6a). Blue boxes indicate Miocene rapid uplift in southern Peru (Saylor & Horton, 2014; Kar et al., 2016).